Bulletin de la Société géologique de France
2017, Volume 188 Issue 4 Pages 27
http://dx.doi.org/10.1051/bsgf/2017189
http://archimer.ifremer.fr/doc/00409/52076/

Les structures en araignée : enregistrement d'échappements de fluide provenant des hydrates de méthane sur la pente continentale du Congo

Spider structures: records of fluid venting from methane hydrates on the Congo continental slope

Casenave Viviane [1, 2, *], Gay Aurélien [1], Imbert Patrice [2]

[1] Géosciences Montpellier, UMR 5243–CC 60, Université Montpellier, 2 , place E.-Bataillon, 34095 Montpellier cedex 05, France
[2] CSTJF, Total, avenue Larribau, 64018 Pau cedex, France

* Corresponding author : Viviane Casenave, email address : viviane_casenave@hotmail.com

Abstract :

Fluid seepage features on the upper continental slope offshore Congo are investigated using multi-disciplinary datasets acquired during several campaigns at sea carried out over the last 15 years. This datasets includes multibeam bathymetry, seismic data, seafloor videos, seafloor samples and chemical analyses of both carbonate samples and of the water column. Combined use of these datasets allows the identification of two distinctive associations of pockmark-like seabed venting structures, located in water depths of 600–700 m and directly above a buried structural high containing known hydrocarbon reservoirs. These two features are called spiders due to the association of large sub-circular depressions (the body) with smaller elongate depressions (the legs). Seismic reflection data show that these two structures correspond to amplitude anomalies located ca. 60–100 ms below seabed. The burial of these anomalies is consistent with the base of the methane hydrate stability domain, which leads to interpret them as patches of hydrate-related bottom-simulating reflection (BSR). The morphology and seismic character of the two structures clearly contrasts with those of the regional background (Morphotype A). The spider structures are composed of two seafloor morphotypes: Morphotype B and Morphotype C. Morphotype B makes flat-bottomed depressions associated with the presence of large bacterial mats without evidence of carbonates. Morphotype C is made of elongated depressions associated with the presence of carbonate pavements and a prolific chemosynthetic benthic life. On that basis of these observations combined with geochemical analyses, the spider structures are interpreted to be linked with methane leakage. Methane leakage within the spider structures varies from one morphotype to another, with a higher activity within the seafloor of Morphotype C; and a lower activity in the seafloor of Morphotype B, which is interpreted to correspond to a domain of relict fluid leakage. This change of the seepage activity is due to deeper changes in gas (or methane) migration corresponding to the progressive upslope migration of fluids. This phenomenon is due to the local formation of gas hydrates that form a barrier allowing the trapping of free gas below in the particular context of the wedge of hydrates.

Résumé

Les caractéristiques des échappements de fluides sur la pente continentale supérieure, au large des côtes du Congo, sont étudiées en utilisant des jeux de données pluridisciplinaires, acquis au cours de plusieurs campagnes marines menées au cours des 15 dernières années. Ces jeux de données comprennent de la bathymétrie multifaisceaux, des données sismiques, des vidéos des fonds marins, des échantillons du fond marin et des analyses chimiques à la fois des échantillons de carbonate et de la colonne d'eau. L'utilisation combinée de ces ensembles de données a permis l'identification sur le fond de l'eau, de deux associations distinctes de structures d'échappements de fluides de type pockmark, localisées entre 600 et 700 m de profondeur d'eau et directement au-dessus d'un haut structural enterré contenant des réservoirs d'hydrocarbures connus. Ces deux structures sont appelées araignées en raison de l'association des grandes dépressions subcirculaires (le corps) avec de petites dépressions allongées (les pattes). Les données de sismique réflexion montrent que ces deux structures correspondent à des anomalies d'amplitude localisées à 60–100 ms en-dessous des fonds marins. L'enfouissement de ces anomalies est compatible avec la base de stabilité des hydrates de méthane, ce qui conduit à les interpréter comme des patchs de Bottom-Simulating Reflection (BSR) reliés à la présence d'hydrates. La morphologie et la nature des deux structures contrastent clairement avec celles de du contexte régional (Morphotype A). Ces structures en araignée sont composées de deux morphotype du fond marin : le Morphotype B et le Morphotype C. Le Morphotype B constitue des dépressions à fond plat associées à la présence de grands tapis bactériens et sans indice de présence de carbonates en fond de mer. Le Morphotype C est constitué de dépressions allongées associées à la présence de croÛtes carbonatées et d'une vie benthique chimio-synthétique prolifique. Sur la base de ces observations, combinées à des analyses géochimiques, les structures en araignée sont interprétées comme étant liées à des fuites de méthane. Les fuites de méthane à l'intérieur de ces structures en araignée varient d'un morphotype à l'autre, avec une activité plus importante dans le fond marin du Morphotype C, et une activité plus faible dans le fond marin du Morphotype B, qui est interprété comme étant un vestige de site d'échappement de fluides. Cette évolution de l'activité d'échappement de fluides est due à des changements plus profonds dans la migration du gaz (ou du méthane), correspondant à la migration progressive des fluides vers le haut de la pente. Ce phénomène est dÛ à la formation locale d'hydrates de gaz qui forment une barrière permettant le piégeage sous-jacent de gaz libre, dans le contexte particulier du biseau des hydrates.

Keywords : methane seep, methane hydrates, bottom-simulating reflector (BSR), dynamic seepage, methane-derived authigenic carbonates (MDAC)

Mots clés : fuite de méthane ; hydrates de méthane ; BSR (*bottom-simulating-reflector*) ; fuite dynamique ; carbonates dérivés du méthane (MDAC)

Introduction

Fluid flow features represent anomalies generated during past and present subsurface flow of fluids (oil, gas, brine, groundwater and magmatic fluids) from source to the seabed or land surface [Cartwright *et al.*, 2007; Løseth *et al.*, 2009]. The type of structure generated depends on a variety of parameters as for instance the source of fluid, the flow type, the structural setting and the nature of the host sediments [Cartwright *et al.*, 2007; Huuse *et al.*, 2010]. Pockmarks, mud volcanoes, gas hydrates, chimneys, pipes, some sediment injections, and some carbonate bodies (e.g methane-derived authigenic carbonates, MDAC), and related diagenetic phenomena are examples of geologic features associated with temporally varying systems of focused fluid seepage through the seabed [Cartwright *et al.*, 2007; Judd &Hovland, 2007; Løseth *et al.*, 2009; Huuse *et al.*, 2010].

Seafloor fluid flow features, such as pockmarks, are commonly found overlying deep or shallow hydrocarbon reservoirs [Heggland, 1998], and along continental margins where they are often associated with localized gas hydrate accumulations [Bünz &Mienert, 2004; Ivanov *et al.*, 2007]. On 3D seismic data, these geologic features are commonly found to be underlain by columnar zones of attenuated and disrupted reflections called “acoustic chimneys” , or “blow-out pipes” [Løseth *et al.*, 2011] depending whether the authors just describe their seismic character or consider them as genuine fluid escape conduits.

Fluid flow features specifically related to methane hydrates and their dynamics have received specific attention over the past decade both for their potential role in climate change [Maslin *et al.,* 2010] and their growing economic interest [Milkov & Sassen, 2002]. Accumulation of gas hydrate below the seafloor occurs either as stratiform accumulation associated with a bottom simulating reflection (BSR) in the subsurface [Shipley *et al.,* 1979] or as shallow gas hydrates accumulations preferentially localized along fault planes [Simonetti *et al.*, 2013] and below pockmarks [Marcon *et al.*, 2014].

The use of high-resolution three-dimensional seismic data brings new insight to the occurrence of gas hydrates, their dynamics of growth and demise, and relationship with venting points and deep plumbing systems. This includes sediment collapse and pockmarks formation due to hydrate dissolution forming specific features called “hydrate pockmarks” [Sultan *et al.*, 2010; Imbert &Ho, 2012; Riboulot *et al*., 2016]; local hydrate accumulations below the seabed forming “hydrate pingoes” [Hovland & Svensen, 2006; Sérié *et al.*, 2012] and hydrate mounds [Matsumoto *et al.*, 2009; Nakajima *et al.*, 2014].

The Lower Congo Basin, offshore SW Africa, is a prolific petroleum province that has been extensively explored for more than 30 years, resulting in a growing quantity and quality of exploration data (Séranne, 1999; Marton *et al.*, 2000; Babonneau *et al.,* 2002; Rouby *et al.*, 2002; Fort *et al.*, 2004; Broucke *et al.,* 2004; Gay *et al.,* 2006a; Andresen *et al.,* 2011; Beglinger *et al.,* 2012). Numerous studies have recognized the widespread occurrence of past and present fluid flow-related phenomena [Andresen *et al.*, 2011; Gay *et al.*, 2007], including the widespread occurrence of gas hydrates [Cunningham & Lindholm, 2000], pockmarks [Andresen *et al.*, 2011; Gay *et al.,* 2006a] and giant pockmarks that correspond to depressions whose diameter exceeds ca. 1000 m wide, generally found in the deep part of the basin [Marcon *et al.,* 2014; Ondréas *et al.,* 2005; Sahling *et al.,* 2008]. Pockmark commonly seems to be closely linked to gas hydrates occurrence either for some small-scale pockmarks deeply rooted with a BSR [Gay *et al.,* 2006a] or for giant pockmarks showing the presence of gas hydrates in the shallow subsurface [Marcon *et al.,* 2014; Ondréas *et al.,* 2005; Sahling *et al.,* 2008].

This study presents the discovery, on the upper part of the slope, of a new type of pockmark-like feature corresponding to seafloor fluid vents. These features are called "spider structures" because they combine a subcircular flat-bottomed pockmark ("body" of the spider) with furrows extending upslope over a distance comparable to the diameter of the pockmark ("legs"). This work is based on a highly diverse array of data that allow the well-constrained characterization of the newly defined spider structures. The results provide a potential insight into the processes of seabed fluid venting in the particular context of the pinch out of the BSR. This work aims to propose a genetic model of fluid migration from depth over time in relation to inferred gas hydrate formation near seabed and ongoing methane seepage. The main contribution of this work concerns how seabed vents record fluid flux through time, a process of which we still have a limited understanding [*e.g.* Foucher *et al.* 2009].

Geological Setting

The investigated area is located in the Lower Congo Basin, on the Congo slope, between 500 m and 1200 m water depth, north of the Congo canyon (Fig.1). The Lower Congo basin is one of many sub-basins along the West African continental margin which was initiated in the early Cretaceous during the opening of the South Atlantic Ocean [Brice *et al.*, 1982; Karner *et al.*, 1997; Marton *et al.*, 2000]. Following the rifting, restricted-marine conditions allowed the deposition of up to 1 km of Aptian evaporites (the Loeme Formation), that constitute the decollement layer responsible for the salt tectonic that characterizes this part of the margin (Fig.2) [Brice *et al.*, 1982; Duval *et al.*, 1992; Liro & Coen, 1995; Lundin, 1992; Valle *et al.*, 2001; Uchupi, 1992]. The gravitational sliding of the sedimentary cover above the salt layer defines an upslope extensional domain characterized by rafts and grabens and a downslope compressive domain characterized by salt diapirs, canopies and walls, each domain being about 100 km wide within the Lower Congo Basin [Duval *et al.*, 1992; Fort *et al.*, 2004; Lundin, 1992; Marton *et al.*, 2000; Rouby *et al.*, 2002]. The study area is located in the extensional domain and is structured into horsts and grabens bounded by listric faults (Fig.2).

The stratigraphy of post-rift sediments consists of two major sequences; these are separated by the Oligocene Unconformity that reflects a major change in ocean circulation and climate [Séranne *et al.*, 1992; Séranne, 1999]. The latter sequence corresponds to the icehouse period that began in the early Oligocene. This sequence has been characterized by an overall regression superimposed by alternating dry and wet climate periods and high amplitude (>100m) high frequency (100 kyr) sea level oscillations [Bartek *et al.,* 1991; Miller *et al.,* 2005; Seranne, 1999; Zachos *et al.,* 2001]. During this period, sedimentation has been dominated by the progradation of a terrigeneous wedge associated with the deep incision of the Congo submarine canyon [Séranne, 1999]. The large amount of terrigeneous material has led to the formation of the large turbidite systems of the Congo fan [Brice *et al.,* 1982; Broucke *et al.,* 2004; Droz *et al.,* 1996; Uchupi, 1992]. Deep thermogenic fluids [Gay *et al.,* 2006a] migrating upward are preferentially trapped in sandy turbidite channel reservoirs. Significant oil and gas discoveries have been made in this basin over the last two decades [Beglinger *et al.,* 2012; Burwood, 1999; Cole *et al.,* 2000]. Since the early Pliocene, the shelf and the slope have been bypassed because of the deep incision of the Congo canyon that directly connects the Congo River with the deep basin and the abyssal plain, down to 4000 m water depth [Babonneau *et al.,* 2002]. As a consequence, the slope, including the study area, has only been receiving sparse amounts of fine-grained sediments along with pelagic production [Jansen *et al.,* 1984; Pufahl *et al.,* 1998; Uenzelmann-Neben, 1998].

The Pliocene-present interval contains widespread fluid escape features, at seabed and in the subsurface, indicating past and ongoing bypass of the regional seal [Andresen *et al.,* 2011; Cartwright, 2011; Gay *et al.,* 2006a], which corresponds to a major polygonal fault system [Cartwright, 2011; Gay et al., 2004].

Data and Methodology

The dataset (Fig.3) includes multibeam bathymetry, seismic data, seafloor videos, seafloor samples geochemistry and chemistry of the water column. All these data have been acquired during several marine campaigns carried out over the last 15 years (Zaiango, 1999; Zairov, 2000, Biozaire, 2001, Total Geohazard, 2011).

Seismic data

The study is based on both 3D seismic volumes and 2D, high resolution (HR) seismic profiles. The seismic interpretation and attribute analyses were performed with the SISMAGE software developed by Total [Guillon & Keskes, 2004]. All data are displayed in two-way travel time (TWT) and values are expressed in s (TWT) or ms TWT. The average velocity in the upper section studied here is estimated at ca. 1500 $m.s^{-1}$ [Sultan *et al.* 2007], so that 100 ms TWT roughly correspond to 75 m.

Exploration and High Resolution (HR) 3D seismic data

Two 3D seismic volumes with a multichannel offset, acquired for hydrocarbon exploration are used for this study (Fig. 3). The first dataset covers about 1900 km^2 with a line spacing of 12.5 m and a CDP distance of 12.5 m. The dominant frequency is 70 Hz in the upper 100 ms TWT, with a significant frequency content up to 80-90 Hz, giving a vertical resolution of ~ 4 m (at a velocity of 1700 $m.s^{-1}$) and a horizontal resolution of ca. 20 m; the vertical sampling is 4 ms TWT. The second dataset is a high-resolution 3D volume covering 120 km^2 with a line spacing of 6.25 m in both directions (in brown on Fig.3) and a sampling rate of 3 ms TWT. The dominant frequency is 70 Hz in the upper 100 ms TWT (similar to the regional survey), but with a significant frequency content up to 100-110 Hz in the upper 100 ms TWT of the sedimentary pile; this gives a vertical resolution of ca. 3 m for a velocity of 1700 $m.s^{-1}$. The seabed signal is not symmetrical, which means that the data are not zero-phase [Brown, 2011]. This study mainly used the amplitude, “dip” and coherence [Bahorich & Farmer, 1995] attributes. The coherency attribute estimates over a window selected by the interpreter the correlation between a seismic trace and the adjacent ones. The “dip” attribute is an approximation of the local slope gradient in degrees; it was calculated here at each sample over the 8 surrounding points.

High resolution 2D-AUV seismic data

High-frequency 2D seismic data with high resolution (HR) and low penetration (2D-AUV and Chirp for example) are generally used to study sub-seafloor anomalies [Orange *et al.,* 1999; Savini *et al.*, 2009]. All AUV data were acquired using C&C's **C-Surveyor I^{TM}**.

Roughly 300 km of High Resolution (HR) 2D-AUV seismic profiles were used for the study (Fig.3). The AUV was equipped with an Edge Tech Chirp Subbottom Profiler. The transmit pulses are generated in the frequency band between 2 and 8 kHz. The high-resolution 2D-AUV seismic profiles have a spacing of 175 m in a SW-NE direction and about 1000 m in the orthogonal direction over the area of interest. The signal has a penetration of about 100 ms TWT and a resolution of 6-10 cm. Due to the low penetration of the high frequency signal, no reflections were identified below around 70 m below the seafloor. These 2D seismic profiles were interpreted using a combination of the recorded amplitude and its "envelope", a moving Root Mean Square (RMS) average.

Seabed bathymetry

Bathymetry data were acquired by the AUV equipped with a Simrad EM 2000 Swath bathymetry system collecting soundings in a 200-meter swath underneath. Multibeam data were processed at a 3-meter bin size using C&C's proprietary HydroMap software and the depth values are referenced to Lowest Astronomical Tide (LAT). Bathymetry data cover an area of about 400 km^2 (Fig. 3) with a horizontal resolution of about 3 m. The vertical resolution provided by the 200 kHz source is a few cm.

Side-Scan Sonar (SSS) data:

Side-Scan sonar data were collected by the AUV equipped with a dual frequency chirp Edge Tech Side Scan Sonar. It uses a calibrated wide band digital frequency modulated (FM) signal to provide high resolution, low-noise images. This sonar simultaneously transmits linearly swept FM pulses centered at two discrete frequencies: 120 kHz and 410 kHz with a maximum cross-track resolution of respectively 6.25 cm and 1.8 cm. The acoustic penetration can reach several meters depending on the sediments at the sea bottom. The backscatter data are used for the impedance contrast detection in the seafloor sediments and in the shallow sub-seafloor. High backscatter intensity is displayed in dark tones (Fig.3).

Seafloor videos and sampling:

Two video transects were acquired during two surveys (Fig.3). The first one (ROV track 1) corresponds to the ZAIANGO IFREMER/TOTAL-FINA-ELF program (Zairov mission in 2000) with the “ROV Victor” (Remote Operated Vehicle). The second one (ROV track 2) corresponds to an industrial geotechnical campaign acquired by SEAROV in 2012 for Total with the “ROV Seaeye Panther”. The last ROV dive has allowed collecting pictures of the seafloor that have never been published yet. The ROV dives were partly dedicated to the sampling of massive carbonate crusts by video-controlled grab on 2 different sites (Fig.3).

Isotopic analyses:

Isotope values of carbon and oxygen were obtained by with the Isotope-Ratio Mass Spectrometry (IRMS) method by the use of a Delta V+ spectrometer after extraction of the CO_2. Analytic precision of measurements is 0.1 ‰ for both $\delta^{18}O$ and $\delta^{13}C$ values. The isotopic ratio of carbon represents the difference between the ^{13}C / ^{12}C values (Table 1) measured on a sample relative to the Pee Dee Belemnite (PDB) international standard. The isotopic ratio of oxygen indicates the difference between the ^{18}O / ^{16}O ratio (Table 1) measured on a sample and an international standard corresponding to the SMOW (Standard Mean Ocean Water).

Water column chemistry:

During the Zairov mission in 2000, water was sampled in several pressurized bottles, in both hydrocasts and ROV sampling, to measure the actual concentrations of dissolved methane and also the concentrations of iron, manganese end silicon dissolved.

Hydrocasts were also carried out using a SBE 9/11+ Seabird conductivity–temperature–depth (CTD) sensor with a Wet Labs nephelometer, at the BZR-01 Station (see Fig.3.B for location). This CTD/rosette was also equipped with 16 pressurized bottles of 8 l capacity in order to sample the water column.

In addition, a Victor ROV dive was carried out above the area of interest, between 550 m to 800 m water depth, in which 15 pressurized minibottles of water were sampled, 3 m above the seabed (Fig.3.B). Aliquots of 125 ml were immediately collected in glass bulbs with Teflon stopcocks and analyzed on board using a chromatographic purge/trap technique [Charlou & Donval, 1993; Charlou *et al.,* 1998]. Aliquots of 60 ml were acidified for Fe and Mn analysis.

Geophysical characterization

Morphology and distribution of seafloor morphotypes

In the Lower Congo Basin, multibeam data were combined with coherency maps derived from 3D seismic data in order to better characterize the seafloor morphology. Two kilometric scale anomalies were identified at about 600-700 m water depth (Fig.4). Three main seafloor morphotypes have been identified:

<u>Morphotype A</u>: The bathymetric and the slope gradient maps only show slight variations of slope angles (Fig. 4A&B). The seafloor is smooth and only a few depressions and mounds are visible in the north-western part. The backscatter reflectivity has an average low value

displayed as a light grey on Fig.4.C. The coherency is high and shows no major variations over the area (Fig.4.D). This morphotype is considered as the background regional seafloor.

Morphotype B: The bathymetric and the gradient maps show two sub-circular flat-bottomed depressions on the seafloor (Fig.4.A&B). They are 2-3 m meters deep on average and are characterized by a rough bottom surrounded by continuous edges. They are both elliptical in shape and their preferential elongation is close to the gradient of the regional NNW-SSE slope. The northwestern depression is approximately 1.5 km long and 1 km wide, representing an area of about 1.2 km^2. The southeastern depression is about 0.7 km long and 0.6 km wide covering a surface of 0.4 km^2. Within the flat depressions the backscatter reflectivity is low (Fig.4.C) and the coherency is generally medium (Fig.4.D). A few lower coherency anomalies are also visible on the coherency map. They appear as isolated irregular to crescent-shaped patches, a few tens of meters in length (Fig.4.D).

Morphotype C: The bathymetric map shows a set of elongated depressions, about 10-m deep (Fig.4.A). They have steep edges with slope angles reaching 35° as shown by Fig.4.B. Nearly 75 % of these elongated depressions trend in a NNW-SSE direction, subparallel to the regional slope gradient. They are very narrow: about 50 m wide for a length ranging from 50 m to 1000 m. Some of the elongated depressions widen into elliptical patches, 200 m long and 100 m wide (Fig.4.A). The backscatter map shows high reflectivity anomalies on the seafloor (Fig.4.C), including a few thin and elongated depressions and six of the broader anomalies corresponding to the elliptical patches described on the slope gradient map (Fig.4.C). Within this Morphotype C, all depressions are very low in coherency (Fig.4.D). Morphotypes B and C are associated in two sets, each comprised of a patch of Morphotype B from whose periphery appear to emanate furrows of Morphotype C. In each set, the distribution of the furrows is strongly skewed towards the SE side of Morphotype B, with the orientation of individual furrows ranging from radial (with respect to Morphotype B) to southeastwards trending, the latter being dominant. For each set, the network of Morphotype C furrows reaches about one diameter of the patch of Morphotype B in a SE direction.

This association of Morphotypes B and C allows defining two main objects on the seafloor: the deeper one is 2.7 km long and 2 km wide and consists of a large patch of Morphotype B, with peripheral furrows of Morphotype C extending southeastwards; shallower on the slope, a similar feature covers 1.2 km in length and 0.7 km in width and also shows furrows developing upslope from a patch of Morphotype B. They are both called "Spider Structures" (SS) as they consist of a main “body” (i.e. sub-circular patch of Morphotype B) and peripheral “legs” (i.e. elongated Morphotype C). The "Spider Structures" are named SS1 (larger feature) and SS2 (smaller) (Fig. 5).

Large amplitude anomalies on seismic sections

The studied seismic interval shows several amplitude anomalies located just underneath the two spider structures previously identified (Fig.6). Two strong amplitude anomalies identified at 1100 ms TWT below seafloor (Fig.6.C) correspond to Miocene turbidite channels that have been exploited for over a decade. They are cut by listric normal faults that compartmentalize the reservoirs. Some of these faults reach the seafloor where they are expressed as curved depressions (Fig.6.A).

Two flat high-amplitude anomalies are also identified in the shallow subsurface just below the two spider structures (Fig.6). Although the used seismic dataset is not zero-phase, the flat reflections can be seen to have a polarity (white/black) opposite to that of the seafloor (black/white) (Fig.6.C.D). These anomalies are almost parallel to the seafloor, slightly converging upslope towards it; in those respects, they fulfill the criteria of BSRs (Bottom

Simulating Reflections) and can thus be suspected to correspond to the Base of the Gas Hydrate Stability Zone (BGHSZ) [e.g. Dillon *et al.,* 1980].

In order to test this interpretation, 5 couples of temperature/pressures have been estimated along the amplitude anomalies on the basis of their depth of occurrence (pressure) and geothermal gradient (temperature). Three gradients were used, based on the three measurements reported in the vicinity [Sultan *et al.,* 2004]: 48 °C/km, 50 °C/km and 56 °C/km. The seabed temperature was estimated as the seabed intercept of Sultan *et al*.'s dataset at about 6.5 °C. The pressure was taken as hydrostatic, in accordance to what is normally observed at shallow depths with normal sedimentation rates [Osborne & Swarbrick, 1997]. Time-depth conversion was carried out using a compressional acoustic velocity (V_p) of 1500 m.s-1 in these very shallow, uncompacted and unlithified lithologies, as measured in previous studies [Sultan *et al.,* 2007]. Figure 7 shows the comparison between the five (P, T°) points estimated along the suspected BSR and hydrate stability curves for variable methane / ethane mixes, from 100 % to 90 % CH4, as reported in [Sloan & Koh, 2007]. There is a good consistency between the burial of the observed reflection and the base of the hydrate stability zone calculated using the locally measured [Sultan *et al.* 2004] for a gas mixture that contains more than 99 % methane. Other combinations like a gas more enriched in C2H6 (more stable) and a higher geotherm (pushing the stability domain upward) could give the same result, but such solutions seem too speculative to be retained in the absence of representative analyses of the gas at BSR level.

These two patches of BSRs are not strictly parallel to the seabed (Fig.6.C&D) but slightly oblique to it, with a depth below the seabed decreasing from 100 to 60 ms TWT in an upslope direction as the seabed shoals from 700 to 600 m water depth (Fig.6.B). Bottom-simulating reflections normally wedge upslope as they approach the wedge of gas hydrates, thereby reducing the thickness of the gas hydrate stability domain [Field & Kvenvolden, 1985]. The tilting of the interpreted BSRs is consistent with the fact that the upslope wedge of gas hydrates is estimated to be located at a water depth around 550 m in the study area [Sultan *et al.,* 2004]. On a map view, the high amplitude anomalies form two patches of BSRs, one covering about 2 km^2 and the other ca. 0.5 km^2 (Fig.6.B)). The wider patch of BSR is located in an area where two faults are connected (Fig.6.A). Both BSR patches are associated with an underlying high amplitude chaotic and discontinuous zone, a few ms to 150 ms TWT thick (Fig.6.c&D). Such anomalies are commonly interpreted as free gas zones below the BSR [Berndt *et al.,* 2004; Bouriak *et al.,* 2000], as the BSR commonly marks the transition between gas hydrate-bearing sediments and the underlying free gas zone [e.g. Dillon *et al.,* 1980]. The dimming of seismic reflections forms two columns of about 1500 ms TWT high and 600 m wide that extend down to the underlying hydrocarbon reservoirs.

Shallow sub-seafloor amplitude anomalies

In the study area, 2D-AUV profiles were used to highlight subsurface anomalies in the first 70 m below seafloor. The 2D-AUV seismic profile CD crosses the main body of Spider Structure 1 from NE to SW (Fig. 8.A; see Fig. 4 for location). The envelope attribute displays high-amplitude seismic anomalies as dark grey patches. Four levels of irregular high-amplitude anomalies were identified in the subsurface right below the main flat-bottom depression of Morphotype B. On both sides of the depression the envelope attribute shows low amplitude parallel and continuous reflections. They correspond to the background seismic Morphotype A in the area, as evidenced on all other 2D-AUV seismic profiles (see Fig. 3 for location).

The two deepest levels, level 1 (60 ms TWT below seafloor) and level 2 (35 ms TWT below seafloor), consist of high-amplitude reflections rather discontinuous, that concentrate under the SW part of Morphotype B (Fig. 8.A). On the contrary, the two shallowest levels, level 3

(25 ms TWT below seafloor) and level 4 (10 ms TWT below seafloor), are present under the whole depression of Morphotype B (Fig. 8.A.B). In contrast with deeper levels, “Level 4” rather appears as an interval, 8 to 12 ms TWT thick, composed of closely spaced amplitude anomalies 30 to 100 m wide each (Fig.8.B).

Figure 8.-C illustrates on a 2D-AUV seismic profile (amplitude display) the relationships between reflections outside the anomalies and inside the patch of Morphotype B. Reflections visible laterally to the depression can be followed below the margin before they fade out. They consistently plunge down slightly towards the center of the depression. This combination of downwarping and progressive loss of amplitude may at first glance evoke diffraction hyperbolae at the edge of background reflections. However, real diffraction hyperbolae are clearly expressed around the main anomalies of level 4 for instance, and have a much steeper slope than the gentle downwarping at issue here. This downwarping can be followed at least down to below level 2 on the SW side of the seismic profile shown in Fig.8.B. The shape of the crest (in particular the location of the highest point) differs from one horizon to the other, as shown on Fig.8.C. This phenomenon indicates that the down-bending is not a seismic artifact but corresponds to a real geological feature.

Figure 9 shows 2D-AUV seismic profile EF (see Fig.4 for location). This profile is parallel to profile CD, and partly crosses Morphotype C. The dominant seismic facies is parallel and continuous [Mitchum *et al.,* 1977]. The seafloor shows 4 depressions, 5 to 8 ms TWT deep (i.e. 3 to 6 m with a water velocity of 1500 $m.s^{-1}$) and 50 to 120 m wide along the section; they are numbered 1 to 4 from SW to NE on Fig.9. Patches of high-amplitude anomalies develop beneath the depressions. Anomalies 1, 2, 3 and 4 are buried at about 6, 20, 4 and 5 ms TWT respectively below the corresponding depressions. They are all associated with an underlying acoustic mask that forms a very steep inverted V-shaped dimming structure. The seismic reflections are disrupted on both sides of the acoustic mask or they are dimmed and shifted downward suggesting a pull-down effect. The outline of the 2D-AUV profile EF is shown by a dotted rectangle (Fig.9.A) on a profile extracted from the 3D cube along the same line. It shows that shallow buried anomalies beneath elongated depressions (Morphotype C) are all located above the BSR that lies about 90 ms TWT below seafloor (Fig.6.D).

Biological and geological characterization at the seafloor

Visual identification of seafloor morphotypes

On the slope of the Lower Congo Basin, two ROV dives were used to investigate Spider Structures 1 and 2 located between 600 m and 700 m water depth. In particular, the ROV tracks crossed both the body (Morphotype B) and the legs (Morphotype C) of SS1 (see ROV tracks on Fig.3 for location) without observing any gas bubbles escaping from the seafloor. Three sites were selected for representative pictures within SS 1 (see Fig.3 for location): Site 1 in the flat-bottomed depression corresponding to Morphotype B, and sites 2 and 3 in the elongated depressions corresponding to Morphotype C.

Morphotype B: Within the flat-bottomed depression, pictures obtained during ROV dives on site 1 (see Fig.3 for location) revealed the presence of white bacterial mats overlying blackish reduced sediments (Fig.10.A). Bacterial mats are discontinuous and consist of several closely spaced patches ranging in size from tens of square centimeters to tens of square meters (Fig.10.A). Bacterial mats are associated with the presence of mostly empty shells of bivalves belonging to the thiotrophic family Vesicomyidae [Ondréas *et al.,* 2005] scattered all over the seafloor (Fig.10.A). Bivalve shells are sometimes grouped together in the periphery of the bacterial mats forming accumulations of empty shells (Fig.10.B) and sometimes associated with living bivalves.

Morphotype C: Within elongated depressions, ROV dives on sites 2 and 3 (see Fig.3 for location) revealed the occurrence of outcropping carbonates, with a variable degree of cementation (Fig.10.C, D, E and F). Carbonate outcrops can form tubular and/or nodular rocks partially or totally buried in the sediment which sparingly outcrop on the seafloor forming domes (Fig.10.C). Carbonate can also outcrop as thicker tabular carbonate pavements with a flat top (Fig.10.D&E). These carbonate crusts form massive slabs that are often tilted (Fig.10.E) and even fractured (Fig.10.D). The tilted crusts are a few cm to a few m in thickness. They cover an area of about a few hundred square meters. The white bacterial mats grew up directly on the carbonate pavements forming small and discontinuous patches (Fig.10.D, E, F), and they can be associated with black reduced sediments at the toe of carbonate pavements (Fig.10.F). An abundant benthic life, such as tubeworms, anemones, Galathea and bivalves, has been identified on and around carbonate crusts as these provide a solid substrate to which sessile organisms can fix (Fig.10.E). Living bivalves and empty shells are scattered all over the seafloor of this area.

Morphology of seafloor carbonates

During the ROV dives, two main types of carbonate were sampled at sites 2 and 3 (see Fig. 3 for location): 1) Carbonate pavements, associated with bivalve shells, are the most common (Fig.11.D&E). They consist of very poorly sorted shell fragments that are slightly cemented together. These carbonate rocks have a high porosity and are quite brittle due to the low amount of cement (Fig.11.A&C); 2) Nodular or tubular carbonates, which are less observed as they are often found buried within the sediment (Fig.10.C). The only tube-shaped carbonate recovered has a central conduit about 1 cm in diameter (Fig.11.B) connected to smaller secondary conduits of variable diameter which appear as small holes along the main tube (Fig.11.D). Nodules and pipes are much indurated and form hard carbonates.

Chemical analyses of carbonates and water samples

Seafloor carbonates isotopic compositions

The isotopic composition of carbon and oxygen were analyzed on four samples taken from seafloor sites 2 and 3 in patches of Morphotype C (see Fig.3 for location). Delta ^{18}O and $\delta^{13}C$ measurements for both sites are displayed on Table 1. The analyses on site 2 were made separately on the cement part and the shell part of the carbonate samples visible on Fig.11.A, and on a bivalve shell taken from the seafloor. The measurement on site 3 was carried out on a carbonate sample visible on Fig.11.C. With negative values of δ13C (-35.5 ‰ on Site 2 and -34.3 ‰ on Site 3 (Table 1), the carbon isotopic compositions on the carbonate cement fraction are nearly the same at both sites. However, the carbon isotopic compositions for the shell fraction of the carbonate sample (Fig.11.A) and for the isolated shell (both at site 2) show a major change, -3.1 ‰ and 2.1 ‰ respectively (Table 1). The $\delta^{18}O$ values for bulk carbonate fractions are in the range of +3.6‰ to +4.1 ‰ for sites 2 and 3 (Table 1).

Near-bottom water chemical analysis

During the ROV dive near-bottom waters were regularly collected 1-2 m above the seafloor from the northwest corner to the southeast corner of the studied area (Fig.12.A). The water samples were then analyzed for dissolved methane (CH_4), iron (Fe), manganese (Mn) and silicon (Si). Measurements 1-2 (about 820 m water depth) and 13-15 (about 550 m water depth) were made 2 km away from the seafloor anomalies. They were sampled over Morphotype A corresponding to the normal background seafloor. Except for point 2, measurements 1, 13, 14 and 15 range from 3 to 6 nmol/l for CH_4, 153,7 to 308,7 nmol/l for Fe, 9 to 16,9 nmol/l for Mn and 22,3 to 31,7 µmol/l for Si (Fig. 12.A and refer to Table 2-B for exact values).

The only measurement made over Morphotype Bat point 3 (Table 2-B) yieleded a CH_4 concentration of 16 nmol/l. Over Morphotype C, CH_4 concentration is higher with an average of 38 nmol/l and reached four times higher values at points 5 and 6 (Table 2-B). Dissolved methane concentrations measured over the Morphotype C of the deeper Spider Structure 1 (samples 4, 5, 6, 7 and 8) are higher than those measured over the Morphotype C of the shallower spider structure 2 (samples 10, 11 and 12) (Fig.12.A, Table 2-B).

Fe and Mn values measured over both Morphotype B and C are comparable to those over Morphotype A (Table2-B), with the exception of a single sample (point 8).

Calibration values are given by silica due to its low solubility in water. With values ranging from 22,3 to 39,1 µmol/l and a slight decrease with water depth, silica concentrations are consistent with dissolved ratios in seawater [Cheong *et al.,* 2014].

Water column chemical analysis

Complementary analyses have been conducted during the cruise. A vertical CTD/rosette was operated in the water column over the seafloor anomaly (See Fig.3.B for location). The deepest measurement is very close to point 5 measured over the seafloor during the ROV dive. The dissolved methane concentration decreases downward reaching a minimum value of 0.7 nmol/l at 540 m water depth (100 m above the seafloor). From this depth and downward the dissolved CH_4 shows a regular increase reaching its highest value of 4.1 nmol/l at 646 m water depth, close to the seafloor (Fig.12.C and Table 2-A).

The Fe and Mn vertical profiles show a slight increase down to about 540 m water depth (Fig.12.B and Table 2-A). From this depth downward the Fe and Mn concentrations increase more rapidly reaching the values of 75,1 nmol/l and 6,4 nmol/l respectively at 653 m water depth, close to the seafloor (Fig.12.B).

Discussion

Spider structures are made of a central depression forming a giant pockmark (Morphotype B) bordered by elongated depressions (Morphotype C) extending dominantly upslope. Flat-bottomed giant pockmarks reminiscent of Morphotype B have been reported in literature from the deeper parts of the Lower Congo Basin [e.g Ondréas *et al.* 2005] and the Western Mediterranean Sea [Ingrassia *et al.,* 2015]. The set of hydrate pockmarks reported by Sultan *et al.,* 2014 in the deep Niger Delta are also flat-bottomed and exceed 500 m in diameter, making them quite similar to the other examples, although they were not formally referred to as "giant" by the authors. These pockmarks appear as isolated fluid flow features in associations of giant pockmarks with peripheral elongated depressions and have not been described yet. However a close look at Figure 1 of Marcon *et al.* (2014) shows 3 or 4 short (ca. 100-m-long) high-reflectivity furrows extending upslope of the giant Regab pockmark, but these are quite inconspicuous and have not been described as such by the authors. They might be seen as "short-legged spider structures" by reference to the example shown here.

In addition, the Spider Structures develop right above the structural culmination of a proven hydrocarbon reservoir, and are underlain by a seismic reflection that has all the characteristics of a hydrate BSR. Those three factors: 1) surface geometry analogue to that of hydrate pockmarks; 2) presence of a BSR underneath and 3) structural setting over a hydrocarbon field strongly suggest that the two observed Spider Structures could result from dysmigration of hydrocarbons from the underlying reservoir. The following discussion will challenge this hypothesis, starting from water column and seabed data and moving progressively down. The following issues will be addressed: do spiders reflect present seepage? The provenance of the fluids and the migration pathways will be discussed as well as the temporal variability and the origin of the pockmark depression. Finally, the resulting interpretation will be developed into a full genetic and evolutionary model of the Spider Structures.

Are Spider Structures seafloor seeps?

Fluid venting activity within the spider structures

Background dissolved methane concentrations in the deep ocean are normally below 0.9 nmol/l [Scranton & Brewer, 1978]. Significantly higher values just above seafloor or in the water column are considered indicative of significant fluid expulsion [Gay *et al.,* 2006b; Sassen *et al.,* 1994, 2001; Suess *et al.,* 1999].

In the study area, three values of methane concentrations were measured away from the two venting sites, two at 3 nmol/l and one at 6 nmol/l. This is higher than values normally found as ocean background [Scranton & Brewer, 1978]. This could be due to the proximity of active sites of gas release and the presence of an active hydrocarbon generating system in the area.

The values observed above Spider Structure 1 (SS 1) and 2 (SS2) are comprised between 16 and 70 nmol/l. This is about 10 to 80 times the upper limit of normal marine background values, and still 4 to 18 times the average value of the local background; however, these values remain about 3 orders of magnitude below the saturation value for the local thermodynamic conditions (ca. 60,000 nmol/l, http://models.kl-edi.ac.cn/models/ch4-sea, from [Duan & Mao, 2006], accessed 2016/06/21). These values indicate an actual anomaly of methane on both spider structures, albeit with a moderate flux, which is consistent with the fact that no gas bubbles release was observed at the seafloor. Such methane concentrations are not as large as those typically found in sites of gas venting, in particular in other parts of the Lower Congo basin [e.g. Ondréas *et al.,* 2005]. These relatively low methane concentrations measured over Morphotype B and C could be due to a progressive release of methane by steady dissolution of BSR hydrates, which are known to act as dynamic systems [Sultan *et al.,* 2014].

Let us now examine the differences between the two spider structures: eight values of CH4 concentration were recorded for Morphotype C, five of them over Spider Structure 1 (SS1) and three over SS2. The two sets are well contrasted, with an average of 50 nmol/l for SS1 and 20 nmol/l for SS2, in each case with pretty well clustered values. This strongly suggests that SS1 is currently more active than SS2.

It is then possible to examine the variability between the two Morphotypes: as mentioned above, only one single value was obtained for Morphotype B, in SS1, at 16 nmol/l. This single value is three times smaller than the average recorded over Morphotype C in the same SS1. In order to better assess the significance of this contrast, we compared the ROV observations made on Morphotypes B and C. Measurements of CH4 concentrations capture one moment in time, and it is known that venting is an episodic phenomenon [Tryon *et al.,* 1999]. On the contrary, sustaining benthic life requires steady supply of nutrients (methane for chemosynthetic communities). The observation at the seafloor of bacterial mats in Morphotype B, and an active benthic life combined with carbonate pavements in Morphotype C indicates sustained gas venting at both sites.

One hydrocast collected water samples above Morphotype C at various water depths (Fig.12). Dissolved methane decreases regularly upward from the lowest measurement up to ca. 550 m, which is interpreted to reflect the presence of a methane plume undergoing progressive dilution upwards. The lower 2 measurements have CH4 concentrations of ca. 4 nmol/l, about 9 times what is considered as the upper limit normal oceanic background [Scranton & Brewer, 1978]. Above 550 m, the values steadily increase upwards, a classical behavior in surface waters as methane is a product of metabolism in the intestinal tract of zooplankton and fish [Dafner *et al.,* 1998 ; Lamontagne *et al.,* 1973 ; Oremland, 1979]. The hydrocast also recorded iron and manganese concentrations, which are well correlated with CH4 in the lower part influenced by the plume. On board ROV measurements, 1-2 m above the seafloor, showed localized peaks of dissolved methane concentrations above both Morphotype B and C; this indicates that localized points of emission may be active simultaneously in both morphotypes; however methane venting is much more active over Morphotype C rather than over Morphotype B. The seepage sites have thus fed distinct methane plumes all contributing to a much larger plume identified in the water column using the hydrocast.

Although Fe and Mn concentrations seem to be correlated with methane venting in the hydrocast record, they do not show significant correlation with the dissolved methane concentration at the seafloor over Morphotypes B and C. The rapid oxidation of iron in the water column can explain the fact that iron concentrations at dissolved methane emission points are sometimes close to the ocean background, suggesting that such gas vents have a variable and maybe a lower activity. On the contrary, the high iron concentrations could correspond to an active gas plume with a steady flow. The in situ production/oxidation of methane can be coupled to the cycling of Mn [Sujith *et al.,* 2014]. The high concentration of Mn in pore water probably suggests the participation of subsurface microorganisms in the geochemical cycling of diverse substrates and their active involvement in the release of Mn [Lovley, 1991]. It could also be attributed to the slower rate of oxidation compared to that of reduction in anoxic sediments [Yadav, 1996]. Dissolved CH_4-Fe-Mn anomalies are the result of fluid seepage into the water column forming a 110-m plume (Fig.12.B.C).

Based on the chemical analyses in bottom seawater and in the water column (hydrocasts), Spider Structures 1 and 2 can be considered as large seafloor seeps resulting from the clustering of u numerous smaller seepage sites, as shown for the Haakon Mosby Mud

Volcano [Milkov *et al.,* 2004; Vogt *et al.,* 1997], in the Barents Sea [Lammers *et al.,* 1995], on the Cascadia Margin [Suess *et al.,* 1999] and in the Lower Congo Basin [Charlou *et al.,* 2003; Gay *et al.,* 2006b].

Flux vs. carbonate development

Having established that the Spider Structures are sites of methane seepage, we will now address the issue of the spatial variability of methane flux, based both on the measured concentrations that reflect instantaneous flux and on the absence / presence / type of benthic communities of seep carbonates, which both inform on the mid-term flux.

First and foremost, in what conditions can methane seep up to the seabed? In normal subseafloor conditions without external input of dissolved methane, the sediment pile shows a bacterial zonation in which bacteria live on less and less energetically efficient redox pairs with increasing depth below seabed. The deepest zone corresponds to methanogenesis, while the one just above is the sulfate reduction zone. Dissolved methane generated by microbial activity is typically consumed within sediment by anaerobic oxidation coupled with reduction of sulfate diffusing from sea water at the interface between these two zones, known as the Sulfate-Methane Transition Zone (SMTZ). The SMTZ typically lies a few meters to a few tens of meters below seabed in normal conditions. The reaction is mediated by a Bacteria / Archaea consortium that produces hydrogen sulfide and HCO_3^- [Boetius *et al.,* 2000; Orphan *et al.,* 2001; Reeburgh, 1976; Valentine & Reeburgh, 2000].

When dissolved methane is actively supplied from deeper zones, its flux can result in the consumption of the entire sulfate available in the shallow section, so that the SMTZ may be pushed up to the seabed by dissolved methane in excess. In that case, dissolved methane can feed benthic life and escape into the water column [Gay *et al.,* 2006a], as observed in the Spider Structures.

As shown by Figures 4.C and 8.B, the regional background (Morphotype A) shows neither seabed reflectivity nor amplitude anomalies in the subbottom, indicating that the limited methane flux observed there is insufficient to promote any significant carbonate development.

The more moderate CH_4 concentrations associated with bacterial mats observed over Morphotype B indicate moderate and possibly episodic fluxes of dissolved methane there. This ongoing venting of gas can only sustain the growth of microbial mats and locally of bivalve communities; conversely, the higher concentrations observed above Morphotype C attest to a higher and likely more permanent flux there, resulting in the development of thriving biological communities [Gay *et al.,* 2006b]. The presence of carbonates over Morphotype C implies that even if the measured methane concentrations are quite low, compared for instance to what has been observed on the Regab pockmark (10 to 100 times higher) in the same basin [Ondréas *et al.,* 2005], methane fluxes must have been high and sustained enough over a long time to allow the formation of the massive carbonates observed on Morphotype C for instance (Fig. 10D, 10E, 10F). On the contrary, the low concentrations of dissolved methane recorded above Morphotype A are clearly insufficient to promote the development of carbonate precipitation at the seabed. Overall, the comparison between CH_4 concentrations and the presence or absence of carbonates on Morphotypes A, B and C is interpreted to indicate that significant carbonate bodies can only develop at the seabed in conditions of high and steady enough methane supply.

Origin of fluids

The next issue is the provenance of the seeping methane; it will be addressed using the isotope analyses of the carbon and oxygen of the carbonates. First, the carbon isotopic composition of authigenic carbonates serves as an indicator for the origin of carbon incorporated during carbonate precipitation [Anderson & Arthur, 1983; Reeburgh, 1980; Ritger *et al.,* 1987].

The carbon isotope composition ($\delta^{13}C$) of shell fractions collected at sites 2 and 3 on Morphotype C (see Fig.3 for location) are -3.1 ‰ and 2.1 ‰ (Fig.13). These values are very close to the shell group defined by [Campbell, 2006], indicating that the carbon corresponds to dissolved inorganic carbon from seawater [Campbell, 2006; Judd & Hovland, 2007]. The two cement fractions of carbonate samples collected on Morphotype C have a very similar carbon isotopic composition with negative values of $\delta^{13}C$: -35.5 ‰ at site 2 and -34.3 ‰ at site 3 (Fig.13).

According to Aharon *et al.,* 1997 and Whiticar, 1999, sources of carbon to the pore fluids include (1) biogenic methane ($\delta^{13}C$ <–65 ‰ PDB) or thermogenic methane ($\delta^{13}C$ from –30 ‰ to –50 ‰); (2) sedimentary organic carbon ($\delta^{13}C$ ~ –25 ‰); and (3) marine biogenic carbonate or seawater CO_3^{2-} with a $\delta^{13}C$ value close to 0 ‰. The amount of mixing between these different sources will determine the $\delta^{13}C$ value of any authigenic carbonate [Paull *et al.,* 1992]. According to [Campbell, 2006], the $\delta^{13}C$ value close to -35‰ measured on studied samples is located at the junction of three possible carbon sources (1) sedimentary organic diagenesis (-15 ‰< $\delta^{13}C$<-35 ‰), (2) oil fractions (-20 ‰< $\delta^{13}C$<-35 ‰) and (3) thermogenic methane (-40 ‰< $\delta^{13}C$<-50 ‰) (Fig.13). Although the measured values of $\delta^{13}C$ are not conclusive by themselves here: they are compatible with an origin from thermogenic hydrocarbons, but also from a combination of biogenic methane and normal marine carbonates.

The stable oxygen isotopic composition of authigenic carbonates provides further information about environmental conditions such as the fluid source and temperature during precipitation [Han *et al.,* 2004; Kim *et al.* 2007]. Carbonate precipitation is accompanied by a temperature-dependent oxygen isotope fractionation relative to the water from which the carbonates precipitate. The $\delta^{18}O$ carbonate isotope analyses of the four samples show homogeneous values close to 4 ‰ V-SMOW (from 3.6 to 4.3 ‰, Fig.13, Table 1), with no significant variations at sites 2 and 3 indicating uniform conditions during carbonate growth at the seafloor. According to Rohling, 2013, the values of $\delta^{18}O$ in surface water range worldwide between -7 ‰ in polar waters and +2 ‰ in tropical waters, and the values along the west coast of Africa lie between + 0.5 and +1 ‰. In that respect, the observed values around +4 ‰ are anomalous. Such anomalously positive $\delta^{18}O$ value of 4 ‰ V-SMOW have commonly been observed in seep carbonates resulting from gas hydrate dissociation [Bohrmann *et al.,* 1998; Feng *et al.,* 2010 ; Greinert *et al.,* 2001; Haas *et al.,* 2010]. This is due to the fact that the water in the gas hydrate cages is enriched in ^{18}O by 2 ‰ to 3 ‰ relative to the primary pore-waters [Davidson *et al.,* 1983; Ussler & Paull, 1995]. The positive anomaly of $\delta^{18}O$ measured at both sites can thus be related to gas hydrate dissolution in underlying sediments.

Isotopic analyses are therefore not conclusive as regards the origin of the seeping methane; in other terms, both thermogenic hydrocarbons coming from the deep and biogenic gas generated in the shallow section could fuel the Spider Structures. The main indication for the distribution of dissolved methane in the area is provided by the two patches of BSR underneath the two Spider Structures (Fig.6). They are located right above two underlying vertical zones of reduced amplitude connecting at depth with Miocene turbidite channels (Fig.6). Hydrates are stable only in dissolved methane-saturated water [Lapham *et al.,* 2010], i.e. in the presence of a continuous flux of gas (dissolved at saturation level or in gaseous state). Local generation of biogenic gas in the shallow section is not supported by any seismic observation, and it seems difficult to envision the presence of localized patches of organic matter in the hemipelagic context of the Pliocene of the area [Uenzelmann-Neben, 1998]. The most likely source for the seeping methane is thus the underlying Miocene reservoir. The next section will discuss the possible migration pathway for the methane from the reservoir up to the Spider Structures.

Fluid pathways

The presence of gas hydrates (whose formation requires active methane supply) just above the local culmination of the underlying hydrocarbon reservoir, and there only, strongly suggests that methane is actively migrating vertically up from the Miocene reservoirs to the BSR (but not necessarily as free gas). There are two main pathways for fluids through a sedimentary column, along fault planes and within fluid pipes [Gay et al., 2007].

In the study area, major normal faults are associated with slight linear depressions on the seafloor (Fig.3&6). However, they are not directly related to gas venting sites, except where they cross Miocene turbidite channels at depth. Here, deep-rooted faults individualized several half-grabens (Fig.6). The two patches of BSR and the two related seafloor seep sites are located over the crest of a horst block forming local culminations of the Miocene reservoirs. This suggests that the structural tops of the Miocene reservoirs act as leakage points for upward hydrocarbon migration. Some high-amplitude anomalies have been identified at variable levels at depth along major fault planes with variable polarities and may represent seep carbonates indicating past occurrence of gas seepage along some of the faults (positive amplitudes) or minor gas accumulations trapped in local reservoirs (negative patches).

The Pliocene to Present interval is highly affected by polygonal faulting [Gay *et al.,* 2004]. Polygonal faults may act as migration conduits for driving up fluids entrapped within underlying sandy reservoirs [Gay *et al.,* 2004; Lonergan *et al.,* 2000], it has recently been argued that they could also seal early after burial in the same Lower Congo Basin, on the basis of a detailed analysis of the geometric relationships between high impedance seismic anomalies and polygonal fault pairs [Ho et *al.*, 2016]. There is no clear evidence on our dataset that these faults played any role in the formation of the Spider Structures in the area.

Both patches of BSR are partly underlain by columns of low-amplitude, commonly fuzzy reflections down to the top of the Miocene reservoirs; locally, these columns slightly widen downward (Fig.6.B). They could correspond either to an acoustic masking effect by the shallow free gas trapped under the BSR, or real evidence for the presence of free gas bubbles attenuating the signal. The only difference between these two hypotheses is the thickness of free-gas-bearing sediment: a few meters or tens of meters in the former, or the full column from reservoir to BSR in the latter. The seismic cube was processed for amplitude vs. offset studies (AVO), and both short and long offset cubes are available. Undershooting by far seismic offsets should narrow down the masking window at depth, while a continuous gas column down to the reservoir should have the same geometry on short and long offset data. A comparison of short and long offset cubes was undertaken, but did not prove conclusive due to the differences in frequency content between the two cubes.

Whatever the case, the patches of BSR match the local culminations of the underlying reservoirs. If the gas migrated along the normal faults that affect the series, i.e. along oblique surfaces with a dip of ca. 45°, the BSR should be offset in the upslope direction of the faults. This is not the case, so that fault control on gas migration is negligible. As mentioned in the previous section, independent in situ generation of biogenic gas in the section overlying the reservoirs would imply that patches of source rock were deposited right above the culmination of the underlying reservoirs, which does not seem to make sense. We therefore conclude that gas migrated vertically upward through the seal, without being affected by faults.

Methane seepage evolution over geological time

Buried carbonates and seabed fluid fluxes in Morphotype B

The envelope display of a 2D-AUV profile across Morphotype B shows closely spaced patches of high amplitude buried within the first 60 ms TWT below the main seafloor depression of Morphotype B (Fig.8.A&B). In fluid venting zones, on siliciclastic mud-dominated slopes, positive high amplitude patches on seismic data are generally interpreted as the response of buried carbonate concretions [Bayon *et al.,* 2009; Ho *et al.,* 2012; Römer *et al.,* 2014; Savini *et al.,* 2009].These patches thus seem to correspond to buried seep carbonates that mainly concentrate along four laterally discontinuous levels under the depression of Morphotype B (Fig.8). The distribution of amplitude anomalies into four levels suggests that fluid venting activity has been recently higher than at the present day [Stakes *et al.,* 1999], with periods of massive dissolved gas release alternating with periods of low to very low seafloor fluid venting, possibly representing self-sealing of the seeps [Gay *et al.,* 2006b; Hovland, 2002]. The four levels of amplitude patches are not present on each high-resolution 2D seismic profile, and each level has a different lateral extension. The two deepest levels concentrate in the western part of the main depression (Fig.8), meaning that fluid venting was initially more active in this area. The two shallowest levels are more heterogeneous with high to very high amplitude patches (Fig.8). This could indicate zones were gas venting activity was locally higher. This has also been observed in the elongated depressions of Morphotype C, where sites of massive dissolved gas release (Fig.12) were correlated with high amplitude seafloor anomalies on seismic data (Fig.9). The shallowest level, 10 ms TWT thick, is made of densely distributed high amplitude patches. This interval is buried at about 10 ms TWT below seafloor and it was identified on all high resolution 2D seismic profiles crossing Morphotype B. This suggests that the episode of massive dissolved gas release responsible for the formation of this uppermost concretion-bearing interval affected the entire depression of Morphotype B. Morphotype B consists of two ellipsoidal flat-bottomed and 1-3 meters deep depressions with smooth edges (Fig.4.A&B). They are characterized by medium coherency values, indicating a rough bottom or subbottom due to the heterogeneous distribution of the sub-seafloor anomalies. They are also characterized by a very low backscatter reflectivity (Fig.4.C), similar to the regional slope reflectivity. The vertical resolution of the latter tool being a few cm, this means that there is no buried hard structures are present in the first few cm below seafloor in Morphotype B. The bottom of Morphotype B only revealed the presence of wide white patches of bacterial mat settled on black reduced sediments, but neither associated with benthic life, nor with carbonate slabs (Fig.10.A-B). The low concentrations of dissolved methane with relatively low concentrations of dissolved Mn and Fe suggest a rather diffuse and low fluid venting activity. The patch of Morphotype B can thus be considered as a dying site, which is being draped by hemipelagic sediments and currently undergoing a low gas venting activity with low and probably discontinuous release of dissolved methane in the water column.

Seabed carbonates and fluid fluxes in Morphotype C

Where 2D-AUV profiles cross elongated depressions of Morphotype C, the seismic profiles show high amplitude patches located in the immediate sub-seafloor section (Fig.9). The size of these high-amplitude patches mostly depends on the width of the associated seafloor elongated depressions. The high amplitude patches visible on seismic data, are usually associated with an underlying acoustic blanking effect (Fig.9), which is quite commonplace on high-resolution shallow seismic profiles in areas where gas is present [Judd & Hovland, 2007]. At the seafloor, Morphotype C is characterized by low values of coherency (Fig.4.-D), and high values of backscatter reflectivity, more particularly in the broadest depressions (Fig.4.C). This means that there is a significant contrast in lithology between the regional slope made of hemipelagic sediments and the bottom of elongated depressions. The in-situ seafloor observations obtained during ROV dives confirmed that the depressions of Morphotype C correspond to carbonates as massive slabs, nodules and tubes with a central conduit (Fig.10.C to 10.F, Fig.11); the distribution of carbonates matches the extent of the high-coherency and high-reflectivity depressions. The authigenic carbonates of Morphotype C are associated with the extensive occurrence of microbial mats on blackish reduced, flat sediments outcropping between carbonate concretions (Fig.10.F), indicating widespread intense hydrocarbon seepage and active microbial dissolved methane conversion via anaerobic oxidation of methane [Römer *et al.,* 2014]. Carbonate slabs can form massive and large slabs many of which are tilted; this leads to the exhumation of a part of the slab while the other part is buried in the surrounding hemipelagic sediments (Fig.10.D-E). Most of these slabs, besides being tilted, are fractured and form several fragments, some of which collapsed onto the mud-covered floor of the adjacent furrow (Fig.10.D). The nodular and tubular carbonates with central conduits are partly buried although they generally form within the sediments suggesting a later erosion of covering hemipelagic sediments (Fig.10.C). The presence of authigenic carbonate slabs associated with an abundant benthic life as tubeworms and bivalves (Fig.10.E) is an indicator for sustained seep activity [Gay *et al.,* 2006b; Macelloni *et al.,* 2013; Olu *et al.*, 2009].

Temporal evolution

The vertical evolution of seismic reflectivity observed in subseafloor from level 1 to level 4 and at the seabed thus indicates that the high flux of dissolved methane seepage was initially concentrated in the western part of Morphotype B and progressively migrated eastwards. It is presently concentrated in Morphotype C, which is located E-SE of Morphotype B. This means that the lateral migration of the fluid seepage, since the emplacement of the deepest anomaly identified at 60 ms TWT below seafloor, has been following the same direction over time corresponding to an E-SE (i.e. upslope) migration of the fluid seepage.

We tried to assess the temporal variation of the fluid venting activity within the spider structure by estimating the sedimentation rate and then the ages of the buried levels of high amplitude under Morphotype B. The Pliocene interval of the study area is approximately 1 s twt thick. We used this assessment to estimate the sedimentation rate during the Pliocene interval, assuming an average velocity of 1800 m/s for the interval. The sedimentation rate with these parameters is estimated at around 20 cm/ky. This value is consistent with the sedimentation rates obtained in the shallower 80 m on ODP (Ocean Drilling Program) well 1076, which is 30 cm/ky. The deepest seismically visible level under Morphotype B (level 1) is located at around 60 ms twt below seafloor, corresponding to around 45 m with a velocity of 1500 m/s in the shallow subsurface [Sultan *et al.* 2007]. Using the locally estimated sedimentation rate, Level 1 is dated at ca. 0.2 Ma, which would indicate that spider structure 1 has been active since the Ionian stage of the Pleistocene.

The shallowest anomaly (level 4) ca. 10 m below seabed could be dated around 50 ka with this estimate. Keeping in mind that the upper 10 m are significantly less compacted than deeper level, this value is likely to be a maximum.

Origin of the depression

Careful picking of the high-resolution 2D-AUV seismic profile crossing Morphotype B has shown that background horizons could be followed into the domain covered by Morphotype

B (the seafloor depression) and that they show some downward bending below the edge of that domain. Figure 8.C indicates that horizons are affected down to below Level 1, suggesting local removal of material over the area of Morphotype B, below the deepest seep carbonate interval (Level 1). Along with the presence of hydrates interpreted from the BSR underneath, this sagging is interpreted to reflect hydrate dissociation and removal like in hydrate pockmarks observed in Nigeria [George & Cauquil, 2007] and documented by [Sultan *et al.,* 2010]. The dimming of the reflections below Morphotype B makes it difficult to see whether sagging occurred in one episode or progressively over time.

Genetic model of the Spider Structure

1. Present-day situation

At present, both Spider Structures exhibit a similar style of venting, with lower activity in Morphotype B and higher activity in Morphotype C. The former is just sufficient to feed microbial mats at the seafloor and give a CH4 concentration in surface sediments that exceeds the local background by a factor 3 or 4. In Morphotype C, CH4 concentration is about 3 times higher than in Morphotype B of the same Spider.

The morphology of the two morphotypes are very contrasted, B being smooth and very uniform whereas Morphotype C shows long furrows separated by plateaus of smooth seabed. Carbonates are widespread at the floor of the furrows and in their banks.

As regards hydrates, Morphotype B is underlain by a continuous patch of BSR, while the BSR is much more subdued and discontinuous below Morphotype C. No BSR can be seen in areas of background Morphotype A.

Morphotype A corresponds to very limited CH4 supply if any, Morphotype B to areas of uniform low flux and Morphotype C to a clustering of linear domains of flux high enough to sustain abundant chemosynthetic life.

Let us now examine the recent evolution of the flux, integrating the shallow subsurface information below Morphotype B.

2. Evolution since the most recent carbonate (from level 4 to present)

Combining now subsurface observations with seafloor observations and analyses, it is possible to propose an evolutionary model depicting the two morphotypes as successive stages of evolution of the leakage system, as follows:

a) Active gas venting activity at the giant pockmark (MB)

In an early phase, methane migrating from the Miocene reached the seabed with fluxes high enough to promote the development of seep carbonates below what is currently Morphotype B (level 4 on Fig.8). Methane hydrates may have started to form during this phase or not; in any case, enough gas was supplied / the BSR was discontinuous enough to let abundant methane pass upwards through it and reach the seabed. Figure 14.A depicts the situation at that time, showing the situation where the hydrate BSR was beginning to form in the area. No venting activity could be recorded below the “legs” of the spiders at that time

b) Upslope shifting of the gas venting activity, from the giant pockmark (MB) to elongated pockmarks (MC)

At a certain point in time, the development of porosity-clogging hydrates was such that upwards migration of methane significantly decreased at Morphotype B, as shown on Fig. 14.B. Methane went on diffusing from the hydrates above the BSR upwards to the seafloor through diffusion, with possibly some additional advective flux along fractures or other preferential pathways. This residual flux is able to sustain the growth of microbial mats, with the local development of small communities of pelecypods, but not to promote the development of widespread full communities as observed on Morphotype C. From this point on, the former seep carbonates were progressively buried by hemipelagic drape that smoothed the seabed over Morphotype B.

The dissolution of hydrates in the lower part of the hydrate stability zone (above the impervious BSR) results in progressive subsidence of the overlying series, forming the seafloor depression. The body of the spider can thus be viewed as a progressively collapsing hydrate pockmark, as described by [Wei *et al.,* 2015] for an active example or [Imbert & Ho, 2012] for a cluster of fossil equivalents

c) Setting of the current gas venting activity in elongated pockmarks (MC)

When there were enough hydrates to significantly decrease methane flux at Morphotype B, incoming methane was redirected below the BSR overall acting as seal and shifted upslope to the area of Morphotype C (Fig. 14.C). Methane venting is currently ongoing there, as evidenced by the thriving biological communities present in and around the furrows, and it has been active long enough for thick carbonate crusts to develop. The furrows are interpreted as the linear equivalent of pockmarks, where leakage is responsible for removal of fine-grained material and excavation of the furrows. The reason of this focusing of dissolved gas along linear features is not clear yet: some furrows appear to follow very shallow faults (less than 100 ms twt deep) while others develop without seismic evidence for a fault, at least with the resolution of the seismic data.

3. Speculative evolution of the fluid venting activity below the giant pockmark (MB), over four carbonate levels

How did the Spider Structures form in the first place? This section will propose a few elements that could guide further reflection about the issue, based on the previous discussed points, the presence of 4 stacked interpreted carbonate levels below Morphotype B and the estimated timing.

The estimate we could make for the full duration of the 4 successive stacked levels of interpreted carbonates underneath Morphotype B is ca. 200 ky. This is clearly to take as an order of magnitude, regarding the uncertainties on the precise rate of sedimentation in the area and its possible fluctuations through time. Using the same estimate, the emplacement of the upper level 4 could be dated around 50 ka. One possibility would be to have the 4 carbonate levels associated with the last 4 major low sea-level stands of the Quaternary ca. 350 ka (MIS 9), ca. 250 ka, ca. 150 ka and ca. 20 ka. [Lobo & Ridente]. We speculate that these may correspond to times when the wedge of hydrates was displaced seaward of the Spider Structures, so that the full methane supply could reach the seabed directly.

Conclusion

Our multidisciplinary study of a site of dissolved methane leakage above a hydrocarbon-bearing reservoir has evidenced a specific type of gas escape feature, undocumented so far. This type of seabed anomaly, here called the "Spider Structure" has the following characteristics:

- A Spider Structure is comprised of a sub-circular, depression ("body" of the spider) from which a set of multi-m-deep furrows ("legs") protrude, dominantly upslope
- In our study area, both the "body" and "legs" leak dissolved methane into the water column, but the "body" shows limited activity while the "legs" are very active.
- The two "spiders" we observed lie above the structural crest of an oil and gas reservoir, some 900 m below; patches of hydrate BSR are visible just below the body of each spider, about 100 m below seabed.

- Visual observation and sampling show carbonates at or just below the seabed in the "legs" of the spiders. Isotopic analysis indicates that these carbonates result from anaerobic oxidation of thermogenic methane.
- The "body" in underlain by at least 4 seismic horizons rich in patches of high-impedance material (interpreted as seep carbonates) in the uppermost 100 m of the sedimentary column.
- These seep carbonate levels are 10 to 20 m apart vertically, the shallowest being ca. 10 m below present-day seabed. The vertical stack is interpreted to reflect temporal variations in the emitted flux of dissolved methane.
- The activity of the seeps has been shifting upslope over time, with early stages essentially developed in the most downslope part of the "body", subsequent ones filling the whole body, while at present the body is moribund and most of the dissolved gas currently leaks from the "legs".
- The shift from "body" to "legs" is interpreted to reflect self-sealing of the hydrate BSR over time, as more dissolved gas is supplied since the base hydrate stability zone (GHSZ) reached its present position at the end of the Holocene transgression. The body still records episodic leakage of low fluxes, reflecting progressive dissolution of the starving upper part of the GHSZ.

This model makes the "Spider Structure" one highly dynamic end-member of the spectrum of hydrate-related leakage features, like hydrate pingoes, mounds and pockmarks. The body is comparable in many respects to hydrate pockmarks described in literature, with a dissociating body at depth leading to some collapse upon hydrate dissolution. The legs could be seen as a precursor stage of the leakage, before hydrate growth makes a continuous layer and clogs the leakage points. A "spider structure" would then be a snapshot of the shift from a dying early activity distributed over a subcircular patch and a later, more juvenile activity restricted to a network of furrows located upslope of the subcircular patch.

The present study has deciphered the recent evolution of the two “Spider Structures” of the area. The study of deeper anomalies on the available 3D seismic surveys should lead to a better understanding of the long-term evolution of the leakage system.

Acknowledgments:

The authors would like to acknowledge Total for the access to seismic dataset and for financing the PhD work of Viviane Casenave. The authors would like to thank Ifremer for the access to the ZAIANGO dataset and Eric Cauquil (TOTAL) for his stimulating insight and encouragements to undertake this study. We also thank Sidonie Révillon for her contribution in carbonate isotopic analysis. We would like to thank the reviewers D. Praeg and N. Sultan for their helpful suggestions and constructive comments.

References

AHARON P., SCHWARCZ H.P. & ROBERTS H.H. (1997). - Radiometric dating of submarine hydrocarbon seeps in the Gulf of Mexico. - *Geological Society of America Bulletin*, **109**, 5, 568-579.

ANDERSON T.F. & ARTHUR M.A. (1983). - Stable isotopes of oxygen and carbon and their applications to sedimentologic and paleoenvironmental problems. *In*: ARTHUR M.A., ANDERSON T.F., KAPLAN I.F., VEIZER J. & LAND L.S., Eds., Stable Isotopes in Sedimentary Geology. - *SEPM Short Course*, **10**.

ANDRESEN K.J., HUUSE M., SCHØDT N.H., CLAUSEN L. F. & SEIDLER L. (2011). - Hydrocarbon plumbing systems of salt minibasins offshore Angola revealed by three-dimensional seismic analysis. - *AAPG Bulletin*, **95**, 1039-1065

BABONNEAU N., SAVOYE B., CREMER M. & KLEIN B. (2002). - Morphology and architecture of the present canyon and channel system of the Zaire deep-sea fan. - *Marine and Petroleum Geology,* **19**, 445- 467.

BAHORICH M. & FARMER, S. (1995). - 3-D seismic discontinuity for faults and stratigraphic features: The coherence cube. - *The Leading Edge*, **14**, 10, 1053-1058

BARTEK L.R., VAIL P.R., ANDERSON J.B., EMMET P.A. & WU, S. (1991). - Effect of Cenozoic ice sheet fluctuations in Antartica on the stratigraphic signature of the Neogene. - *Journal of Geophysical Research*, **96,** B4, 6753–6778.

BAYON G., LONCKE L., DUPRÉ S., CAPRAIS J. C., DUCASSOU E., DUPERRON S., ... & WOODSIDE J. (2009). - Multi-disciplinary investigation of fluid seepage on an unstable margin: the case of the Central Nile deep sea fan. - *Marine Geology*, **261**, 1, 92-104.

BEGLINGER S.E., DOUST H. & CLOETINGH S. (2012). - Relating petroleum system and play development to basin evolution: West African South Atlantic basins. - *Marine and Petroleum Geology,* **30**, 1–25.

BERNDT C., BÜNZ S., CLAYTON T., MIENERT J. & SAUNDERS, M. (2004). - Seismic character of bottom simulating reflectors: Examples from the mid-Norwegian margin. - *Marine and Petroleum Geology,* **21**, 6, 723-733.

BOETIUS A., RAVENSCHLAG K., SCHUBERT C. J., RICKERT D., WIDDEL F., GIESEKE A., ... & PFANNKUCHE O. (2000). - A marine microbial consortium apparently mediating anaerobic oxidation of methane. - *Nature*, **407**, 623-626.

BOHRMANN G., GREINERT J., SUESS E. & TORRES M. (1998). - Authigenic carbonates from the Cascadia subduction zone and their relation to gas hydrate stability. - *Geology*, **26**, 7, 647-650.

BOURIAK S., VANNESTE M. & SAOUTKINE A. (2000). - Inferred gas hydrates and clay diapirs near the Storegga Slide on the southern edge of the Vøring Plateau, offshore Norway. - *Marine Geology*, **163**, 125–148.

BRICE S.E., COCHRAN M.D., PARDO G. & EDWARDS A.D. (1982). - Tectonics and sedimentation of the South Atlantic rift sequences: Cabinda, Angola. - *American Association of Petroleum Geologists Memoir,* **34**, 5-18.

BROUCKE O., TEMPLE F., ROUBY D., ROBIN C., CALASSOU S., NALPAS T. & GUILLOCHEAU F. (2004). - The role of deformation processes on the geometry of mud-dominated turbiditic systems, Oligocene and Lower–Middle Miocene of the Lower Congo Basin (West African Margin). - *Marine and Petroleum Geology,* **21**, 327-348.

BROWN A.R. (2011). – Color, Character and Zero-Phaseness. *In:* BROWN A.R. Ed, Interpretation of three-dimensional seismic data. - *AAPG Memoir 42 and SEG Investigations in Geophysics*, No. 9, 31-61.

BÜNZ S. & MIENERT J. (2004). - Acoustic imaging of gas hydrate and free gas at the Storegga Slide. - *Journal of Geophysical Research ,* **109**, B04102, 1-15.

BURWOOD R. (1999). - Angola: source rock control for Lower Congo Coastal and Kwanza Basin petroleum systems. *In*: CAMERON N.R., BATE R.H. & CLURE V.S., Eds., The Oil and Gas Habitats of the South Atlantic. - *Geological Society of London*, **153**, 181-184.

CAMPBELL K. A. (2006). - Hydrocarbon seep and hydrothermal vent paleoenvironments and paleontology: Past developments and future research directions. - *Palaeogeography, Palaeoclimatology, Palaeoecology*, **232**, 362-407.

CARTWRIGHT J., HUUSE M. & APLIN, A. (2007). - Seal bypass systems. - *AAPG bulletin*, **91**, 8, 1141-1166.

CARTWRIGHT J. (2011). - Diagenetically induced shear failure of fine-grained sediments and the development of polygonal fault systems. - *Marine and Petroleum Geology*, **28**, 1593-1610.

CHARLOU J.-L. & DONVAL J.-P. (1993). - Hydrothermal methane venting between 12°N and 26°N along the Mid-Atlantic Ridge. - *Journal of Geophysical Research*, **98**, 9625-9642.

CHARLOU J. L., FOUQUET Y., BOUGAULT H., DONVAL J. P., ETOUBLEAU J., JEAN-BAPTISTE P., ... & RONA P.A. (1998). - Intense CH 4 plumes generated by serpentinization of ultramafic rocks at the intersection of the 15 20′ N fracture zone and the Mid-Atlantic Ridge. - *Geochimica et Cosmochimica Acta*, **62**, 13, 2323-2333.

CHARLOU J. L., DONVAL J. P., ZITTER T., ROY N., JEAN-BAPTISTE P., FOUCHER J. P., ... & PARTY M. S. (2003). - Evidence of methane venting and geochemistry of brines on mud volcanoes of the eastern Mediterranean Sea. - *Deep Sea Research Part I: Oceanographic Research Papers*, **50**, 8, 941-958.

CHEONG C., NONOSE N., MIURA T. & HIOKI A. (2014). - Improved accuracy of determination of dissolved silicate in seawater using absorption spectrometry. - *Accreditation and Quality Assurance*, **19**, 1, 31-40.

COLE G.A., REQUEJO A.G., ORMEROD D., YU Z. & CLIFFORD A. (2000). - Petroleum geochemical assessment of the Lower Congo Basin. *In*: MELLO M.R. & KATZ B.J., Eds., Petroleum systems of South Atlantic margins. - *American Association of Petroleum Geologists Memoir*, **73**, 325-339.

CUNNINGHAM R. & LINDHOLM R.M. (2000). - Seismic evidence for widespread gas hydrate formation, offshore West Africa. *In*: MELLO M.R. & KATZ B.J., Eds., Petroleum systems of South Atlantic margins. - *American Association of Petroleum Geologists Memoir*, **73**, 93-105.

DAFNER E.N., OBZHIROV A.I. & VERESHZHAGINA O.F. (1998). - Distribution of methane in waters of the Okhotsk and western Bering Seas, and the area of Kuril Islands. - *Hydrobiologia* **362**, 93-101.

DAVIDSON D. W., LEAIST D. G. & HESSE R. (1983). - Oxygen-18 enrichment in the water of a clathrate hydrate. - *Geochimica et Cosmochimica Acta,* **47**, 12, 2293-2295.

DILLON W.P., GROW J.A. & PAULL C.K. (1980). - Unconventional gas hydrate seals may trap gas off southeast U.S. - *Oil and Gas Journal*, **78**, 1, 124-130.

DROZ L., RIGAUT F., COCHONAT P. & TOFANI R. (1996). - Morphology and recent evolution of the Zaire turbidite system (Gulf of Guinea). - *Geological Society of America Bulletin*, **108**, 253–269.

DUAN Z.H. & MAO S.D. (2006); - A thermodynamic model for calculating methane solubility, density and gas phase composition of methane-bearing aqueous fluids from 273 to 523 K and from 1 to 2000 bar. - *Geochim. Cosmochim. Acta.***, 70,** 13, 3369-3386.

DUVAL B., CRAMEZ C. & JACKSON M.P.A. (1992). - Raft tectonics in the Kwanza Basin, Angola. - *Marine and Petroleum Geology*, **9**, 389-404.

FENG D., CHEN D., PECKMANN J. & BOHRMANN G. (2010). - Authigenic carbonates from methane seeps of the northern Congo fan: microbial formation mechanism. - *Marine and Petroleum Geology*, **27**, 4, 748-756.

FIELD M.E. & KVENVOLDEN K.A. (1985). - Gas hydrates on the northern California continental margin. - *Geology*, **13**, 517-520.

FORT X., BRUN J.-P. & CHAUVEL F. (2004). - Contraction induced by block rotation above salt (Angolan margin). - *Marine and Petroleum Geology,* **21**, 1281–1294.

FOUCHER J.P., WESTBROOK G.K., BOETIUS A., CERAMICOLA S., DUPRE S., MASCLE J., MIENERT J., PFANNKUCHE O., PIERRE C. & PRAEG D. (2009) - Structure and drivers of cold seep ecosystems. - *Oceanography*, **22**, 1, 92-109.

GAY A., LOPEZ M., COCHONAT P. & SERMONDADAZ G. (2004). - Polygonal fault-furrows system related to early stages of compaction - upper Miocene to recent sediments of the Lower Congo Basin. - *Basin Research*, **16**, 101–116.

GAY A., LOPEZ M., COCHONAT P., LEVACHÉ D., SERMONDADAZ G. & SERANNE M. (2006a). - Evidences for early to late fluid migration from an upper Miocene turbiditic channel revealed by 3D seismic coupled to geochemical sampling within seafloor pockmarks, Lower Congo Basin. - *Marine and Petroleum Geology*, **23**, 387-399.

GAY A., LOPEZ M., COCHONAT P., SÉRANNE M., LEVACHE D. & SERMONDADAZ G. (2006b). - Isolated sea floor pockmarks linked to BSRs, fluid chimneys, polygonal fault sand stacked Oligocene–Miocene turbiditic paleochannels in the lower Congo Basin. - *Marine Geology*, **226**, 25-40.

GAY A., LOPEZ M., BERNDT C. & SÉRANNE M. (2007). - Geological controls on focused fluid flow associated with seafloor seeps in the Lower Congo Basin. - *Marine Geology*, **244**, 68-92.

GEORGE R.A. & CAUQUIL E. (2007). - AUV Ultra High-Resolution 3D Seismic Technique for Detailed Subsurface Investigations. *In* : Offshore Technology Conference. - *Offshore Technology Conference*. ISBN978-1-55563-254-0

GREINERT J., BOHRMANN G. & SUESS E. (2001). - Gas hydrate-associated carbonates and methane-venting at Hydrate Ridge: classification, distribution and origin of authigenic lithologies. - *Geophysical Monograph-American Geophysical Union*, **124**, 99-114.

GUILLON S. & KESKES N. (2004, October). - Sismage and the 3d visualization at Total. *In*: *American Association of Petroleum Geologists International Conference*: October, 24-27.

HAAS A., PECKMANN J., ELVERT M., SAHLING H. & BOHRMANN G. (2010). - Patterns of carbonate authigenesis at the Kouilou pockmarks on the Congo deep-sea fan. - *Marine Geology*, **268**, 1, 129-136.

HAN X., SUESS E., SAHLING H. & WALLMANN K. (2004). - Fluid venting activity on the Costa Rica margin: new results from authigenic carbonates. - *International Journal of Earth Sciences*, **93**, 4, 596-611.

HEGGLAND R. (1998). - Gas seepage as an indicator of deeper prospective reservoirs. A study based on exploration 3D seismic data. - *Marine and Petroleum Geology*, **15**, 1-9.

HO S., CARTWRIGHT J.A. & IMBERT P. (2012). - Vertical evolution of fluid venting structures in relation to gas flux, in the Neogene-Quaternary of the Lower Congo Basin, Offshore Angola. - *Marine Geology*, **332**, 40-55.

HO, S., CARRUTHERS, D., & IMBERT, P. (2016). -Insights into the permeability of polygonal faults from their intersection geometries with Linear Chimneys: a case study from the Lower Congo Basin. *Carnets Geol*., **16**, 02, 17.

HOVLAND M., GARDNER J. V. & JUDD A.G. (2002). - The significance of pockmarks to understanding fluid flow processes and geohazards. - *Geofluids*, **2**, 127-136.

HOVLAND M. & SVENSEN H. (2006). - Submarine pingoes: Indicators of shallow gas hydrates in a pockmark at Nyegga, Norwegian Sea. - *Marine Geology*, **228**, 15–23.

HUUSE M., JACKSON C. A.-L., VAN RENSBERGEN P., DAVIES R.J., FLEMINGS P.B. & DIXON R.J. (2010). - Subsurface sediment remobilization and fluid flow in sedimentary basins: An overview. - *Basin Research*, **22**, 4, 342-360.

INGRASSIA M., MARTORELLI E., BOSMAN A., MACELLONI L., SPOSATO A. & CHIOCCI F.L. (2015). - The Zannone Giant Pockmark: First evidence of a giant complex seeping structure in shallow-water, central Mediterranean Sea, Italy. - *Marine Geology*, ***363***, 38-51.

IMBERT P. & HO S. (2012). - Seismic-scale funnel-shaped collapse features from the Paleocene-Eocene of the Northwest shelf of Australia. - *Marine Geology*, **332**, 198-221

IVANOV M., BLINOVA V., KOZLOVA E., WESTBROOK G. K., MAZZINI A., MINSHULL T. & NOUZÉ H. (2007). - First sampling of gas hydrate from the Vøring Plateau. - *Eos, Transactions American Geophysical Union*, **88**, 19, 209-212.

JANSEN J.H.F., VAN WEERING T.G.E., GIELES R. & VAN IPEREN J. (1984). - Middle and late Quaternary oceanography and climatology of the Zaire-Congo fan and the adjacent eastern Angola Basin. - *Netherlands Journal of Sea Research*, **17**, 201-241.

JUDD A. & HOVLAND M. (2007). - Seabed Fluid Flow, the Impact on Geology, Biology and the Marine Environment. - Cambridge University Press, Statoil Norway, 290-314.

KARNER G.D., DRISCOLL N.W., MCGINNIS J.P., BRUMBAUGH W.D. & CAMERON N.R. (1997). - Tectonic significance of syn-rift sediment packages across the Gabon–Cabinda continental margin. - *Marine and Petroleum Geology*, **14**, 7, 973-1000.

KIM S. T., O'NEIL J. R., HILLAIRE-MARCEL C. & MUCCI A. (2007). - Oxygen isotope fractionation between synthetic aragonite and water: influence of temperature and Mg 2+ concentration. - *Geochimica et Cosmochimica Acta*, **71**, 19, 4704-4715.

LAMMERS S., SUESS E. & HOVLAND M. (1995). - A large methane plume east of Bear Island (Barents Sea): implications for the marine methane cycle. - *Geologische Rundschau*, **84**, 1, 59-66.

LAMONTAGNE R.A., SWINNERTON J.W., LINNENBOM V.J. & SMITH W.D. (1973). - Methane concentration in various marine environments. - *J. Geophys. Res.* **78**, 5317–5324.

LAPHAM L.L., CHANTON J.P., CHAPMAN R. & MARTENS C.S. (2010). - Methane under-saturated fluids in deep-sea sediments: Implications for gas hydrate stability and rates of dissolution. - *Earth and Planetary Science Letters*, **298**, 3, 275-285.

LIRO L.M. & COEN R. (1995). - Salt deformation history and postsalt structural trends, offshore southern Gabon, West Africa. *In*: JACKSON M.P.A., ROBERTS D.G. & SNELSON S., Eds., Salt tectonics: a global perspective. - *American Association of Petroleum Geologists Memoir*, **65**, 323-331.

LOBO F.J. & RIDENTE D. (2013). - Milankovitch cyclicity in modern continental margins: stratigraphic cycles in terrigenous shelf settings. - *Boletín Geológico y. Minero*, **124***,* 2, 169-185.

LONERGAN L., LEE N., JOHNSON H.D., CARTWRIGHT J.A. & JOLLY R.J. (2000). - Remobilization and Injection in Deepwater Depositional Systems: Implications for Reservoir Architecture and Prediction. *In*: Deep-Water Reservoirs of the World: Gulf Coast Section SEPM Foundation*. - 20th Annual Conference*, Houston, 515-532.

LØSETH H., GADING M. & WENSAAS L. (2009). - Hydrocarbon leakage interpreted on seismic data. - *Marine and Petroleum Geology*, **26**, 7, 1304-1319.

LØSETH H., WENSAAS L., ARNTSEN B., HANKEN N.-M., BASIRE C. & GRAUE K. (2011). - 1000 m long gas blow-out pipes. - *Marine and Petroleum Geology*, **28**, 5, 1047-1060.

LOVLEY D.R. (1991). - Dissimilatory Fe(III) and Mn(IV) reduction. - *Microbiological reviews*, **55**, 2, 259.

LUNDIN E.R. (1992). - Thin-skinned extensional tectonics on a salt detachment, northern Kwanza Basin, Angola. - *Marine and Petroleum Geology*, **9**, 405–411.

MACELLONI L., BRUNNER C.A., CARUSO S., LUTKEN C.B., D'EMIDIO M. & LAPHAM L.L. (2013). - Spatial distribution of seafloor bio-geological and geochemical processes as proxies of fluid flux regime and evolution of a carbonate/hydrates mound, northern Gulf of Mexico. - *Deep Sea Research Part I: Oceanographic Research Papers*, **74**, 25-38.

MARCON Y., ONDRÉAS H., SAHLING H., BOHRMANN G. & OLU K. (2014). - Fluid flow regimes and growth of a giant pockmark. - *Geology,* **42**, 1, 63-66

MARTON L.G., TARI G.C. & LEHMANN C.T. (2000). - Evolution of the Angolan passive margin, West Africa, with emphasis on post-salt structural style. *Geophysical Monograph-American Geophysical Union*, ***115***, 129-150.

MATSUMOTO R., OKUDA Y., HIRUTA A., TOMARU H., TAKEUCHI E., SANNO R., SUZUKI M., TSUCHINAGA K., ISHIDA Y., ISHIZAKI O., TAKEUCHI R., KOMATSUBARA J., FREIRE A.F., MACHIYAMA H., AOYAMA C., JOSHIMA M., HIROMATSU M., SNYNDER G., NUMANAMI H., SATOH M., MATOBA Y., NAKAGAWA H., KAKUWA Y., OGIHARA S., YANAGAWA K., SUNAMURA M., GOTO T., LU H. & KOBAYASHI T. (2009). - Formation and collapse of gas hydrate deposits in high methane flux area of the Joetsu Basin, eastern margin of Japan. - *Journal of Geography*, **118**, 1, 43-71.

MASLIN M., OWEN M., BETTS R., DAY S., DUNKLEY JONES T. & RIDGWELL A. (2010). - Gas hydrates: Past and future geohazard?- *Philosophical Transactions of the Royal Society of London A: Mathematical, Physical and Engineering Sciences*, **368**, 1919, 2369–2393.

MILKOV A.V. & SASSEN R. (2002) - Economic geology of offshore gas hydrate accumulations and provinces - *Marine and Petroleum Geology*, **19**, 1–11.

MILKOV A.V., VOGT P.R., CRANE K., LEIN A.Y., SASSEN R. & CHERKASHEV G.A. (2004). - Geological, geochemical, and microbial processes at the hydrate-bearing Hakon Mosby mud volcano: a review. - *Chemical Geology*, **205**, 347-366.

MILLER K.G., KOMINZ M.A., BROWNING J.V., WRIGHT J.D., MOUNTAIN G.S., KATZ M.E., SUGARMAN P.J., CRAMER B.S., CHRISTIE-BLICK N. & PEKAR S.F. (2005). - The Phanerozoic record of global sea-level change. – *Science*, **310**, 1293–1298.

MITCHUM JR R.M., VAIL P.R. & THOMPSON III S. (1977). - Seismic stratigraphy and global changes of sea level: Part 2. The depositional sequence as a basic unit for stratigraphic analysis: Section 2. Application of seismic reflection configuration to stratigraphic interpretation.- , 53-62

NAKAJIMA T., KAKUWA Y., YASUDOMI Y., ITAKI T., MOTOYAMA I., TOMIYAMA T., MACHIYAMA H., KATAYAMA H., OKITSU O., MORITA S., TANAHASHI M. & MATSUMOTO R. (2014). - Formation of pockmarks and submarine canyons associated with dissociation of gas hydrates on the Joetsu Knoll, eastern margin of the Sea of Japan. - *Journal of Asian Earth Sciences*, **90**, 228-242.

OLU K., CAPRAIS J.C., GALERON J., CAUSSE R., VON COSEL R., BUDZINSKI H., ... & SIBUET M. (2009). - Influence of seep emission on the non-symbiont-bearing fauna and vagrant species at an active giant pockmark in the Gulf of Guinea (Congo–Angola margin). - *Deep Sea Research Part II: Topical Studies in Oceanography*, **56**, 23, 2380-2393.

ONDREAS H., OLU K., FOUQUET Y., CHARLOU J.L., GAY A., DENNIELOU B., ... & SIBUET M. (2005). - Integrated "in situ" study of a deep giant pockmark on the Congo-Angola margin. - *Geo-Marine Letters*, **25**, 5, 281-292.

ORANGE D.L., ANGELL M.M. & LAPP D. (1999). - Using seafloor mapping (bathymetry and backscatter) and high resolution sub-bottom profiling for both exploration and production: detecting seeps, mapping geohazards, and managing data overload with GIS. - *Offshore Technology Conference*.

OREMLAND R.S. (1979). - Methanogenic activity in plankton samples and fish intestines: a mechanism for in situ methanogenesis in oceanic surface water. - *Limnol. Oceanogr.* **24**, 1136-1141.

ORPHAN V.J., HINRICHS K.U., USSLER W I.I.I., PAULL C.K., TAYLOR L.T., SYLVA S.P., ... & DELONG E.F. (2001). - Comparative analysis of methane-oxidizing archaea and sulfate-reducing bacteria in anoxic marine sediments. - *Applied and Environmental Microbiology*, **67**, 4, 1922-1934.

OSBORNE, M. J. & SWARBRICK, R. E. (1997). Mechanisms for generating overpressure in sedimentary basins: a reevaluation. *AAPG bulletin*, **81**, 6, 1023-1041.

PAULL C.K., CHANTON J.P., NEUMANN A.C., COSTON J.A. & MARTENS C.S. (1992). - Indicators of methane-derived carbonates and chemosynthetic organic carbon deposits: examples from the Florida escarpment. *In*: BEAUCHAMP B. & VON BITTER P., Eds., Chemosynthesis: Geological Processes and Products. - *Soc. Econ. Paleontol. Mineral.*, 361–375.

PUFAHL P.K., MASLIN M.A., ANDERSON L., BRÜCHERT V., JANSEN F., LIN H., PEREZ M., VIDAL L. & SHIPBOARD SCIENTIFIC PARTY (1998). - Lithostratigraphic summary for Leg 175: Angola–Benguela upwelling system. *In*: *Proceedings Ocean Drilling Program, Initial Reports*, **175**, 533-542.

REEBURGH W. S. (1976). - Methane consumption in Cariaco Trench waters and sediments. - *Earth and Planetary Science Letters*, **28**, 337-344.

REEBURGH W.S. (1980). - Anaerobic methane oxidation: rate depth distribution in Skan Bay sediments. - *Earth and Planetary Science Letters*, **47**, 3, 345-352.

RIBOULOT, V., SULTAN, N., IMBERT, P., & KER , S. (2016) - Initiation of gas-hydrate pockmark in deep-water Nigeria: Geo-mechanical analysis and modeling. *Earth and Planetary Science Letters*, **434**, 252-263.

RITGER S., CARSON B. & SUESS E. (1987). - Methane-derived authigenic carbonates formed by subduction-induced pore water expulsion along the Oregon/Washington margin. - *GSA bulletin*, **98**, 147-156.

ROHLING, E.J. (2013) -Oxygen Isotope Composition of Seawater. In: Elias S.A. (ed.) *The Encyclopedia of Quaternary Science* **2**, 915-922. Amsterdam: Elsevier.

RÖMER M., SAHLING H., PAPE T., DOS SANTOS FERREIRA C., WENZHÖFER F., BOETIUS, A., & BOHRMANN G. (2014). - Methane fluxes and carbonate deposits at a cold seep area of the Central Nile Deep Sea Fan, Eastern Mediterranean Sea. - *Marine Geology*, **347**, 27-42.

ROUBY D., RAILLARD S., GUILLOCHEAU F., BOUROULLEC R. & NALPAS T. (2002). - Kinematics of a growth fault/raft system on the West African margin using 3-D restoration. - *Journal of Structural Geology*, **24**, 783–796.

SAHLING H., BOHRMANN G., SPIESS V., BIALAS J., BREITZKE M., IVANOV M., KASTEN S., KRASTEL S. & SCHNEIDER R. (2008) - Pockmarks in the Northern Congo Fan area, SW Africa: Complex seafloor features shaped by fluid flow. - *Marine Geology*, **249**, 206-225.

SASSEN R., MACDONALD I. R., REQUEJO A.G., GUINASSO JR N.L., KENNICUTT II M.C., SWEET S.T. & BROOKS J.M. (1994). - Organic geochemistry of sediments from chemosynthetic communities, Gulf of Mexico slope. - *Geo-Marine Letters*, **14**, 110-119.

SAVINI A., MALINVERNO E., ETIOPE G., TESSAROLO C. & CORSELLI, C. (2009). - Shallow seep-related seafloor features along the Malta plateau (Sicily channel–Mediterranean Sea): Morphologies and geo-environmental control of their distribution. - *Marine and Petroleum Geology*, **26**, 9, 1831-1848.SCRANTON M. & BREWER P.G. (1978). - Consumption of dissolved methane in the deep ocean. - *Limnol. Oceanol.,* **15**, 1978, 883–886

SÉRANNE M., SÉGURET M. & FAUCHIER M. (1992). - Seismic super-units and post-rift evolution of the continental passive margin of southern Gabon. - *Bulletin de la Société Géologique de France*, **163**, 2, 135–146.

SÉRANNE M. (1999). - Early Oligocene stratigraphic turnover on the west Africa continental margin: a signature of the Tertiary greenhouse-to-icehouse transition? - *Terra Nova*, **11**, 135-140.

SÉRIÉ C., HUUSE M. & SCHØDT N.H. (2012). - Gas hydrate pingoes: Deep seafloor evidence of focused fluid flow on continental margins. - *Geology*, **40**, 3, 207-210.

SHIPLEY T.H., HOUSTON M.H., BUFFL ER R.T., SHAUB F.J., MCMILLEN K.J., LADD J.W. & WORZEL J.L. (1979) - Seismic evidence for widespread possible gas hydrate horizons on continental slopes and rises. - *American Association of Petroleum Geologists Bulletin*, **63**, 2204-2213.

SIMONETTI A., KNAPP J.H., SLEEPER K., LUTKEN C.B., MACELLONI L. & KNAPP C.C. (2013). - Spatial distribution of gas hydrates from high-resolution seismic and core data, Woolsey Mound, Northern Gulf of Mexico. - *Marine and Petroleum Geology*, **44**, 21-33.

SLOAN E.D. & KOH C.A (2007) - Clathrate Hydrates of Natural Gases. *Third Edition, CRC Press*., 364-394.

STAKES D.S., ORANGE D., PADUAN J.B., SALAMY K.A. & MAHER N. (1999). - Cold-seeps and authigenic carbonate formation in Monterey Bay, California. - *Marine Geology*, **159**, 1, 93-109.

SUESS E., TORRES M.E., BOHRMANN G., COLLIER R.W., GREINERT J., LINKE P., ... & ZULEGER E. (1999). - Gas hydrate destabilization: enhanced dewatering, benthic material turnover and large methane plumes at the Cascadia convergent margin. - *Earth and Planetary Science Letters*, **170**, 1, 1-15.

SUJITH P.P., GONSALVES M.J.B.D., RAJKUMAR V. & SHEBA V.M. (2014). - Manganese cycling and its implication on methane related processes in the Andaman continental slope sediments. - *Marine and Petroleum Geology*, **58**, 254-264.

SULTAN N., FOUCHER J.P, COCHONAT P., TONNERRE T., BOURILLET J.F., ONDREAS H., CAUQUIL E. & GRAULS D. (2004). - Dynamics of gas hydrate: case of the Congo continental slope. - *Marine Geology*, **206**, 1, 1-18.

SULTAN N., VOISSET M., MARSSET T., VERNANT A.M, CAUQUIL E., COLLIAT J.L & CURINIER V. (2007). - Detection of free gas and gas hydrate based on 3D seismic data and cone penetration testing: An example from the Nigerian Continental Slope. - *Marine Geology,* **240,** 1-4, 235-255.

SULTAN N., MARSSET B., KER S., MARSSET T., VOISSET M., VERNANT A.-M., BAYON G., CAUQUIL E., ADAMY J., COLLIAT J.-L. & DRAPEAU D. (2010). - Hydrate dissolution as a potential mechanism for pockmark formation in the Niger delta. - *Journal of Geophysical Research: Solid Earth (1978–2012)*, **115**, B8.

SULTAN N., BOHRMANN G., RUFFINE L., PAPE T., RIBOULOT V., COLLIAT J. L., ... & MARSSET T. (2014). - Pockmark formation and evolution in deep water Nigeria: Rapid hydrate growth versus slow hydrate dissolution. - *Journal of Geophysical Research: Solid Earth*, ***119*****,** 4, 2679-2694.

TRYON M.D., BROWN K.M., TORRES M.E. TRÉHU A.M., MCMANUS J. & COLLIER R.W. (1999). - Measurements of transience and downward fluid flow near episodic methane gas vents, Hydrate Ridge, Cascadia. - *Geology*, **27**, 12, 1075-1078.

UCHUPI E. (1992). - Angola Basin: geohistory and construction of the Continental Rise. *In:* POAG C.W. & DE GRACIANSKY P.C., Eds., Geologic Evolution of Atlantic Continental Rises. - *Van Nostrain Reinhold*, New York, 77–99.

UENZELMANN-NEBEN G. (1998). - Neogene sedimentation history of the Congo Fan. - *Marine and Petroleum Geology*, **15**, 635–650.

USSLER III W. & PAULL C.K. (1995). - Effects of ion exclusion and isotopic fractionation on pore water geochemistry during gas hydrate formation and decomposition. - *Geo-Marine Letters,* **15**, 1, 37-44.

VALENTINE D.L. & REEBURGH W.S. (2000). - New perspectives on anaerobic methane oxidation. - *Environmental Microbiology*, **2**, 5, 477-484.

VALLE P.J., GJELBERG J.G., HELLAND-HANSEN W. (2001). - Tectonostratigraphic development in the eastern Lower Congo Basin, offshore Angola, West Africa. - *Marine and Petroleum Geology*, **18**, 909-927.

WEI J., PAPE T., SULTAN N., COLLIAT J.-L., HIMMLER T., RUFFINE L., DE PRUNELE A., DENNIELOU B., GARZIGLIA S., MARSSET T., PETERS C.A., RABIU A., BOHRMANN G. (2015). - Gas hydrate distributions in sediments of pockmarks from the Nigerian margin – Results and interpretation from shallow drilling. - *Marine and Petroleum Geology*, **59,** 359-370.

WHITICAR M. J. (1999). - Carbon and hydrogen isotope systematics of bacterial formation and oxidation of methane. - *Chemical Geology*, **161**, 1, 291-314.

YADAV D.N. (1996). - Manganese mobilization from the western continental margin of India. - *Current Science-Bangalore,* **71**, 900-905.

ZACHOS J., PAGANI M., SLOAN L., THOMAS E. & BILLUPS K. (2001). - Trends, rhythms, and aberrations in global climate 65 Ma to Present. - *Science*, **292**, 686–693.

Fig.1: Bathymetric map of the Lower Congo Basin from EM12 multibeam acquisition (Zaïango project, 1998-2000) showing the location of the study area, on the upper part of the slope.

Fig. 2: Regional geoseismic section across the West African Margin illustrating the general stratigraphic architecture and salt tectonics (location on Fig. 1), modified from Babonneau *et al.,* 2002.

Fig.3: A. Two-way time map of the seafloor with dip overlain showing the 2D and 3D seismic coverage and the area covered by side-scan sonar (red rectangle). **B.** Bathymetric map of the area of interest with the two ROV tracks (orange and purple) and the two sites where carbonates were sampled.

Fig.4: A. Bathymetric map of the seafloor showing Morphotype A which is characterized by a smooth and regular morphology; Morphotype B, which is rougher and slightly depressed and Morphotype C, which consists of elongate depressions. **B**. Color-coded dip of the seabed calculated from the 3D two-way time map of the seafloor. Both Morphotype A and Morphotype B just show the regional dip, while Morphotype C is marked by high dips that correspond to the margins of the elongated depressions. **C.** Seabed reflectivity from the side scan sonar data showing Morphotype A and B with a low reflectivity, whereas Morphotype C is strongly reflective, indicating a higher acoustic impedance. Reflectivity highlights a series of elliptical patches that develop along the depressions of Morphotype C. **D**. Coherency map of the seabed from 3D seismic data highlighting the difference between Morphotype A (highest coherency), Morphotype B with an intermediate coherency (especially in the NW patch) and Morphotype C, with a very low coherency.

Fig.5: Morphotypes distribution from the compilation of the maps of Fig. 5. This composite map highlights the presence of two similar structures, each composed of a subcircular patch

of Morphotype B with a set of peripheral elongated depressions (Morphotype C) dominantly extending to the SE of the patch.

Fig.6: **A**. Map of the seabed reflectivity showing the two spiders structures (SS1 and SS2), the major normal faults and the location of the 2 seismic lines AB and CD. **B.** Isopach map of the interval between the seafloor and the BSR, showing that the BSR is distributed in two patches and that it is shallower in the SE than in the NE. **C.** Seismic section AB (see Fig.3 for location) from the HR 3D volume, showing the two tilted BSRs associated with a strong amplitude decrease and a distortion of reflections underneath. The seabed shows an asymmetrical “red over black” signal, meaning that the seismic is not zero-phase [Brown, 2011]; conversely, the BSRs appear as “black over red”, i.e. with the opposite polarity. The set of high amplitudes at depth is known to correspond to hydrocarbon-bearing reservoirs. **D.** Seismic section CD (see Fig.5.A for location) showing the tilted BSR and its correspondence with each morphotypes A, B and C at the seafloor.

Fig.7: Gas hydrates stability diagram for both pure methane and different proportions of methane (methane + ethane mixture) [from Sloan and Koh, 2007] on which are plotted several couples of temperature/pressure points corresponding to the observed patches of BSR. Calculation of the temperature at the BSR was made with 3 geothermal gradients obtained close to the structure of interest [Sultan *et al.,* 2004].

Fig.8: Seismic sections (location shown on figure 5) across the main patch of Morphotype B. **A.** Insert from 3D seismic data to show the context above the BSR. **B.** Close-up of the zone shown on A with a white rectangle on 2D-AUV data (envelope display, see text). This high-resolution display highlights the gentle depression associated with Morphotype B, and shows 4 levels of discontinuous sets of aligned reflections underneath, vertically spaced by 10 to 20 ms. The signal labeled “direct arrival” at the top is a seismic acquisition artifact and

not a geological reflection. **C.** Amplitude display of the same seismic profile as B over the SW margin of the depression showing reflection geometry down to below level 1. Seven horizons have been picked and show downwarping below the margin of the depression. The two vertical seismic profiles show the exact location of the rim of the depression (left) and its lowest point (right). The highest point of the picked horizons is not perfectly aligned with the rim, showing that these horizons are not multiples. A number of diffraction hyperbolae can be seen (white circles) where the aligned reflections were observed on 7B. They all show the same curvature, idealized in the box labeled “DH”. The curvature of the NE edges of the picked horizons is much gentler, indicating that the reflections correspond to the presence and morphology of real reflectors in subsurface. Vertical scale is in seconds TWT.

Fig.9: A. Seismic section from 3D seismic data for the context (location shown on Fig.5) across the elongated depressions of Morphotype C, shown in a white rectangle. **B.** Section from 2D-AUV seismic data (envelope display). The seismic profile shows high-amplitude anomalies below each of the depressions, with the deepest anomaly below the gentlest surface depression.

Fig.10: Seafloor pictures from submersible dives, taken on three sites of Morphotypes B and C (locations shown on Fig.3). **A**. Bacterial mats (white patches) associated with black reduced sediments and empty shells of bivalves. **B**. Accumulation of empty bivalve shells scattered on hemipelagic sediments. **C.** Small mount formed by carbonate tubes popping through soft mud. **D.** Flat-topped carbonate crust with a conical shape emerging from the mud, which is highly broken, and crabs walking over. **E.** Flat-topped ‘tabular carbonate crust’, showing a high porosity with living tubeworms and crabs. **F.** Scrappy carbonate crust with white bacterial mats associated with black reduced sediments in between.

Fig. 11: Carbonate samples recovered from sites 2 (A, B, D) and 3 (C). **A.** Shell fragments, very heterogeneous in size, poorly cemented and showing a very high porosity. **B**. Section through a tubular carbonate showing the presence of a central conduit connected to peripheral conduits of smaller diameter. **C**. Crumbly carbonate made of cemented shell fragments with a high porosity**. D.** Well indurated tubular carbonate.

Fig.12: Geochemical data. **A**. Concentrations of dissolved methane, iron and manganese measure: very close to the seabed, along the ROV track over Morphotypes A, B and C. Bathymetry in background. **B**. Vertical evolution of iron and manganese concentrations in the water column above station BZR01 (location on Fig. 3). **C**. Same as B for methane.

Fig.13: Distribution of carbonate samples, recovered over Morphotype C (on sites 2 and 3), in a $\delta^{13}C$ vs. $\delta^{18}O$ diagram showing the possible sources of carbon [modified from Campbell, 200].)

Fig.14: Schematic evolution of the Spider Structures in relationship with a cycle of methane input linked with the dynamic of the gas hydrate formation. **A. (above)**: Incipient methane supply, the gas starts feeding the BSR but high fluxes reach the seabed and feed an active fluid vent associated with well-developed seep carbonates. **B. (centre)**: The BSR is fully developed and plugs the porosity, so that continuously incoming methane cannot reach the seafloor as before, but it is diverted upslope and starts spilling over to the east. **C. (below)**: As methane spills over upslope, it allows the gradual growth of the BSR upslope. Methane starts escaping to the surface making the elongated depressions of Morphotype C that correspond to the active methane venting sites.

Table 1: Isotopic analysis (^{13}C and ^{18}O) made on carbonates samples recovered over Morphotype C on site 2 and 3. Samples analyzed on site 2 correspond to the cement fraction (C-c2) and the shell fraction (C-Sh2) of a carbonate sample of Fig.10.A, and an empty shell of bivalve (Sh2). The sample analyzed on site 3 corresponds to a carbonate (Carb3) of Fig.10.C.

Table 2: Concentrations of dissolved methane, iron, manganese and silica measured 1 to 2 m above the seabed along the ROV track. These concentrations have been measured at 15 points in Morphotypes A, B and C, and evidence high lateral variability.

Fig.1 :

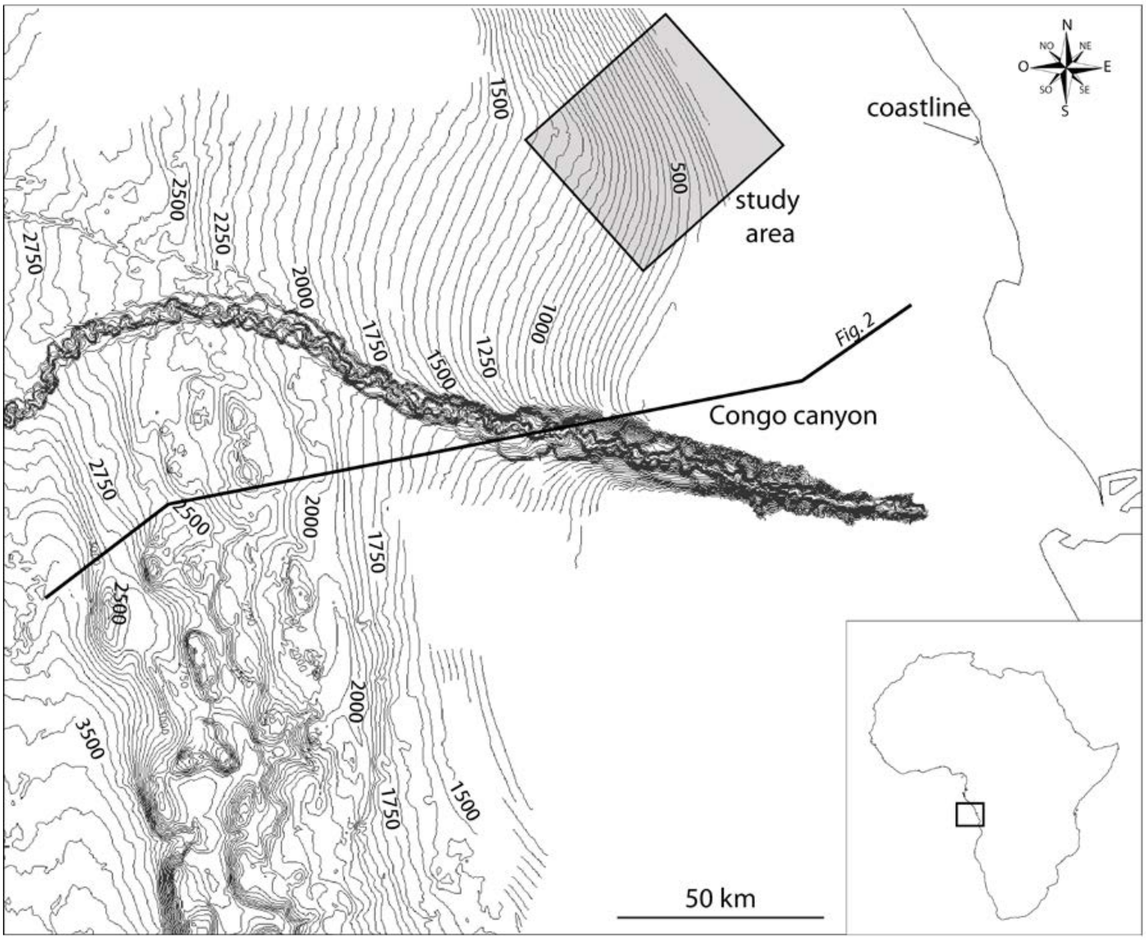
N
NO
NE
O
E
SO
SE
S
coastline
study
area
500
1500
2500
2250
2750
2000
1750
1500
1250
1000
Fig. 2
Congo canyon
2750
2500
2000
1750
2500
3500
2000
1750
1500
50 km

Fig.2

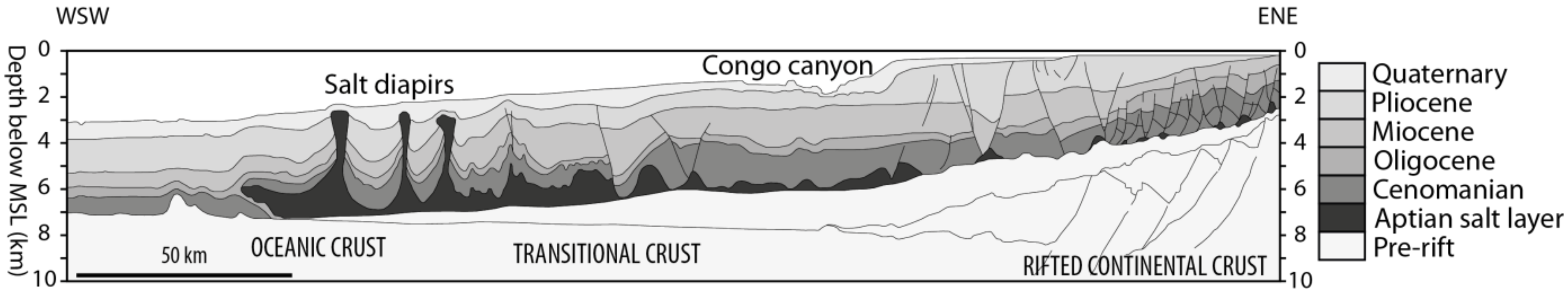
WSW
ENE
Depth below MSL (km)
0
2
4
6
8
10
Salt diapirs
Congo canyon
50 km
OCEANIC CRUST
TRANSITIONAL CRUST
RIFTED CONTINENTAL CRUST
Quaternary
Pliocene
Miocene
Oligocene
Cenomanian
Aptian salt layer
Pre-rift

Fig.3:

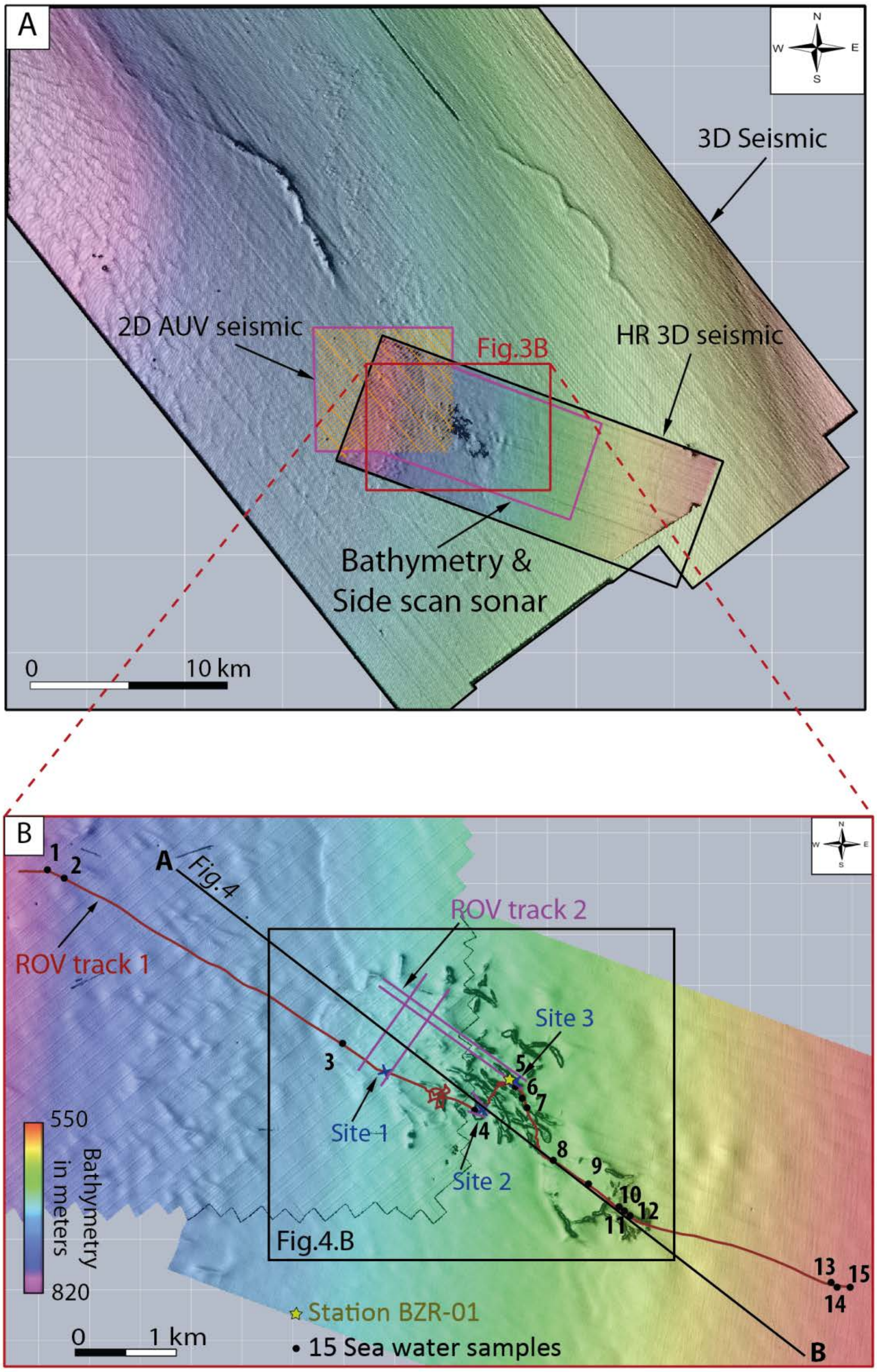
A
N
W
E
S
3D Seismic
2D AUV seismic
Fig.3B
HR 3D seismic
Bathymetry &
Side scan sonar
0
10 km
B
1
2
A
Fig.4
ROV track 2
ROV track 1
Site 3
3
5
6
7
Site 1
4
Site 2
8
9
10
11
12
550
Bathymetry in meters
820
Fig.4.B
13
14
15
Station BZR-01
15 Sea water samples
0
1 km
B

Fig.4:

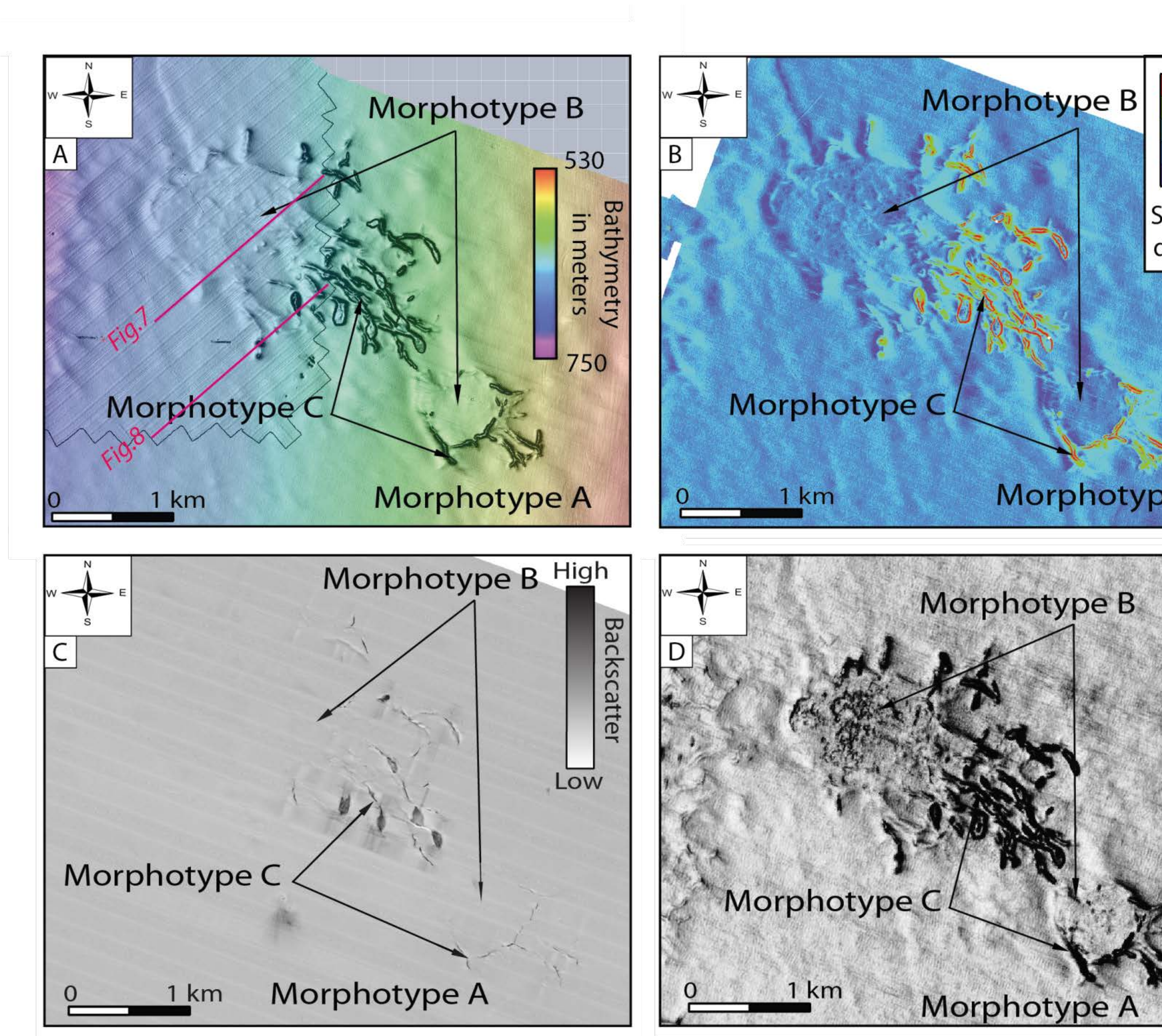

A
N
W
E
S
Morphotype B
530
Bathymetry in meters
750
Fig.7
Fig.8
Morphotype C
0
1 km
Morphotype A
B
Morphotype B
Morphotype C
0
1 km
C
Morphotype B
High
Backscatter
Low
Morphotype C
0
1 km
Morphotype A
D
Morphotype B
Morphotype C
0
1 km
Morphotype A

Fig.5

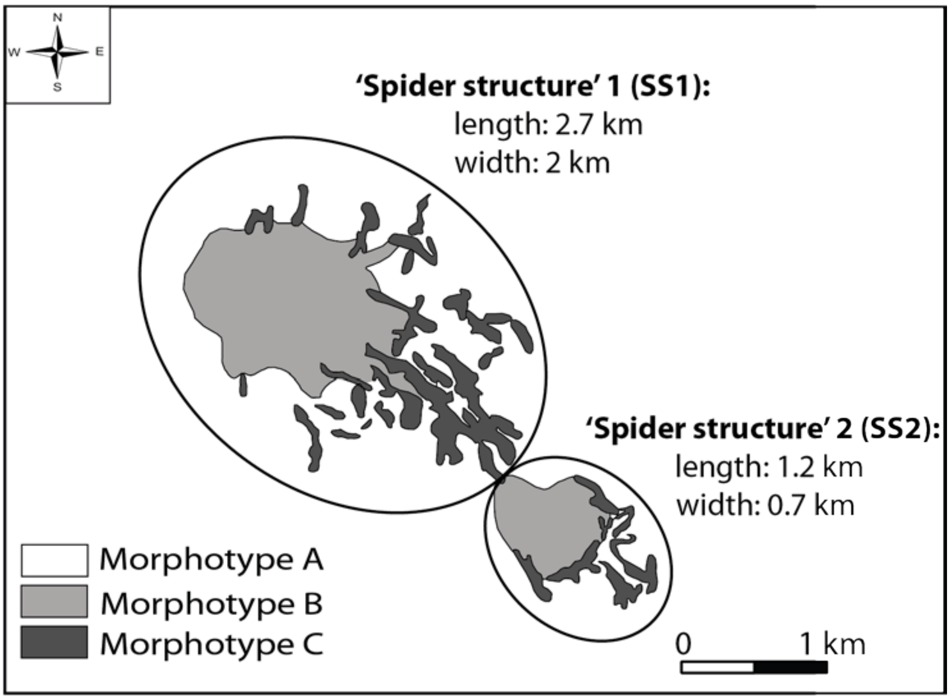
N
W
E
S
'Spider structure' 1 (SS1):
length: 2.7 km
width: 2 km
'Spider structure' 2 (SS2):
length: 1.2 km
width: 0.7 km
Morphotype A
Morphotype B
Morphotype C
0
1 km

Fig.6:

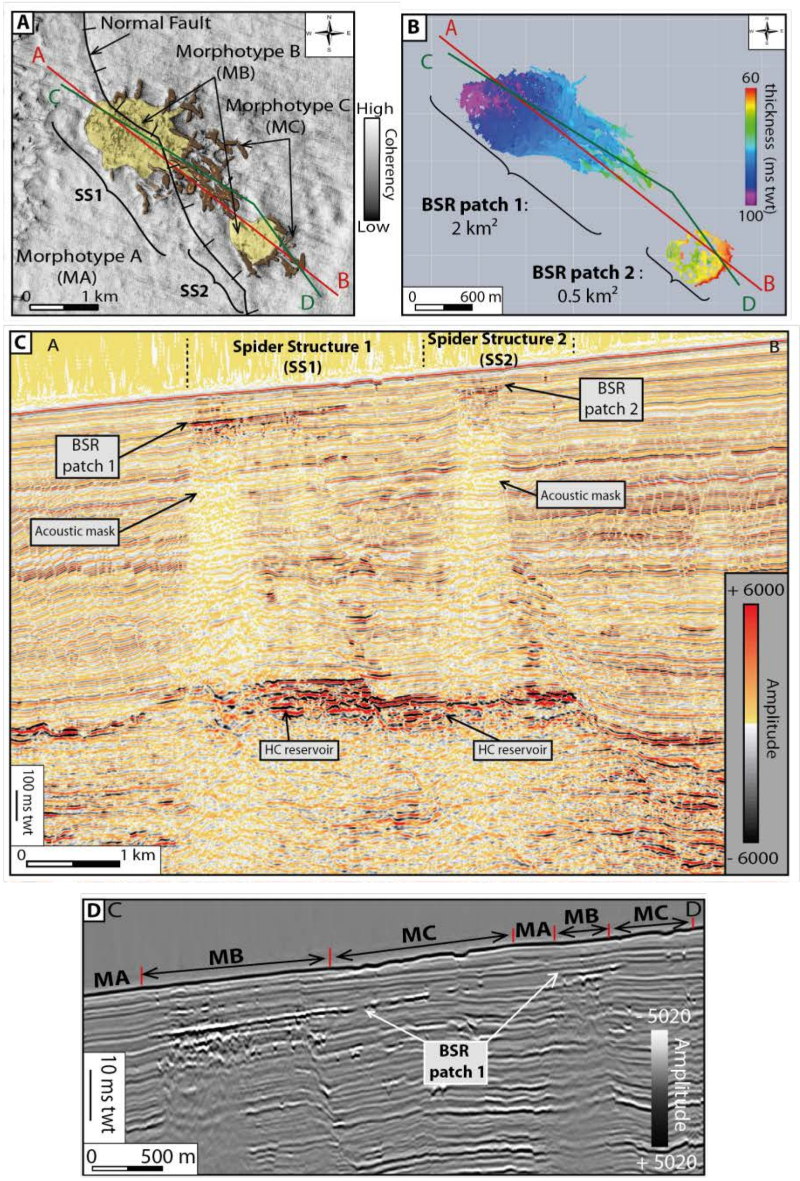
A
Normal Fault
Morphotype B
(MB)
Morphotype C
(MC)
High
Coherency
Low
A
C
SS1
SS2
Morphotype A
(MA)
0
1 km
D
B
B
A
C
60
thickness (ms twt)
100
BSR patch 1:
2 km²
BSR patch 2 :
0.5 km²
0
600 m
D
B
C
A
Spider Structure 1
(SS1)
Spider Structure 2
(SS2)
B
BSR
patch 2
BSR
patch 1
Acoustic mask
Acoustic mask
+ 6000
Amplitude
- 6000
HC reservoir
HC reservoir
100 ms twt
0
1 km
D
C
D
MA
MB
MC
MA
MB
MC
BSR
patch 1
- 5020
Amplitude
+ 5020
10 ms twt
0
500 m

Fig.7:

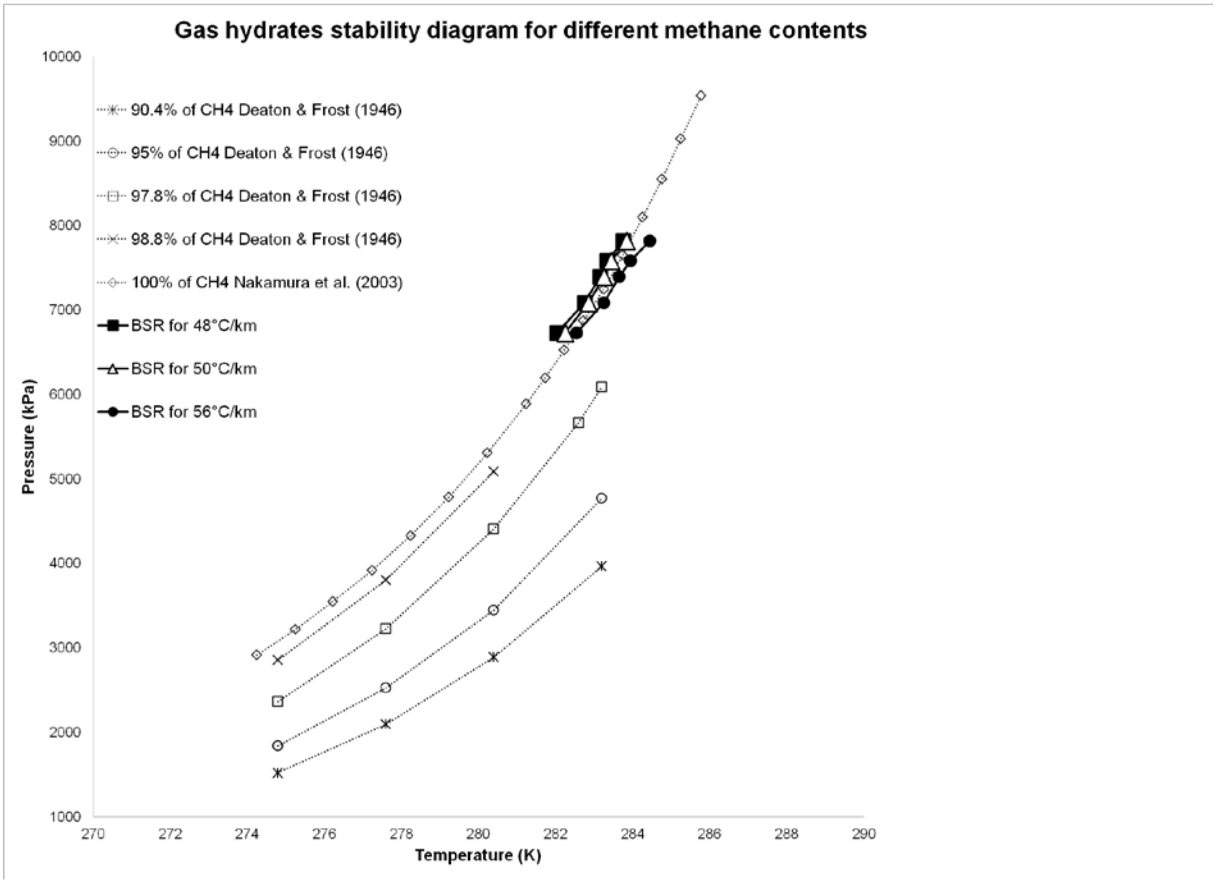

Gas hydrates stability diagram for different methane contents
90.4% of CH4 Deaton & Frost (1946)
95% of CH4 Deaton & Frost (1946)
97.8% of CH4 Deaton & Frost (1946)
98.8% of CH4 Deaton & Frost (1946)
100% of CH4 Nakamura et al. (2003)
BSR for 48°C/km
BSR for 50°C/km
BSR for 56°C/km
Pressure (kPa)
Temperature (K)
10000
9000
8000
7000
6000
5000
4000
3000
2000
1000
270
272
274
276
278
280
282
284
286
288
290

Fig.8:

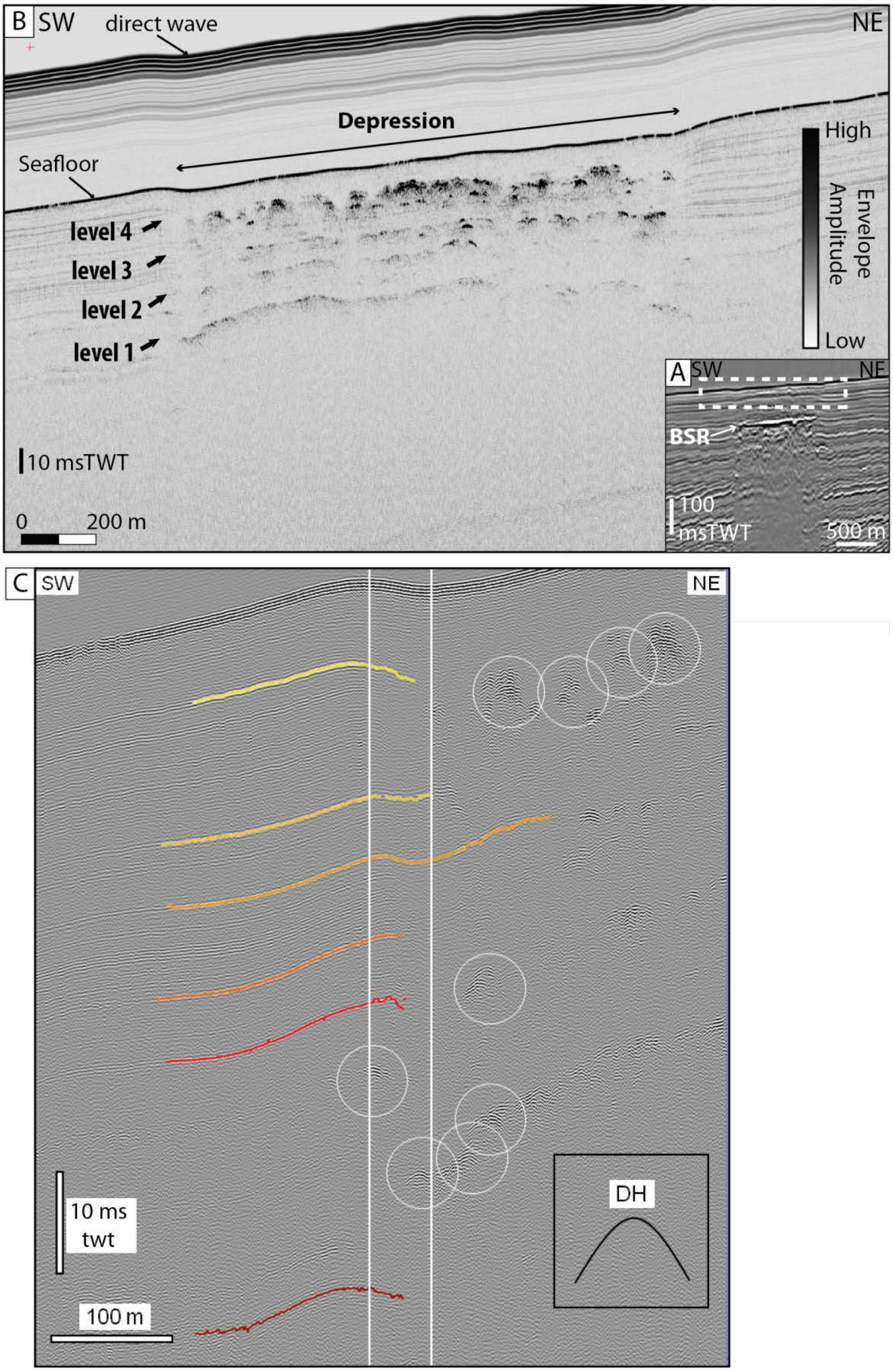
B
SW
direct wave
NE
Depression
High
Envelope Amplitude
Low
Seafloor
level 4
level 3
level 2
level 1
A
SW
NE
BSR
100 msTWT
500 m
10 msTWT
0
200 m
C
SW
NE
DH
10 ms twt
100 m

Fig.9:

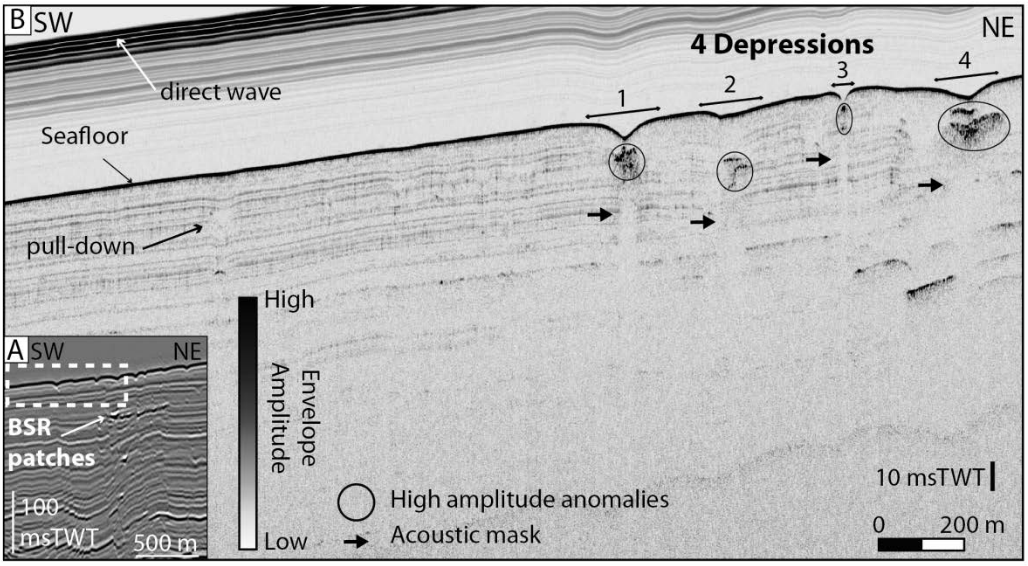
B
SW
NE
4 Depressions
1
2
3
4
direct wave
Seafloor
pull-down
High
Envelope Amplitude
Low
A
SW
NE
BSR patches
100 msTWT
500 m
High amplitude anomalies
Acoustic mask
10 msTWT
0
200 m

Fig.10:

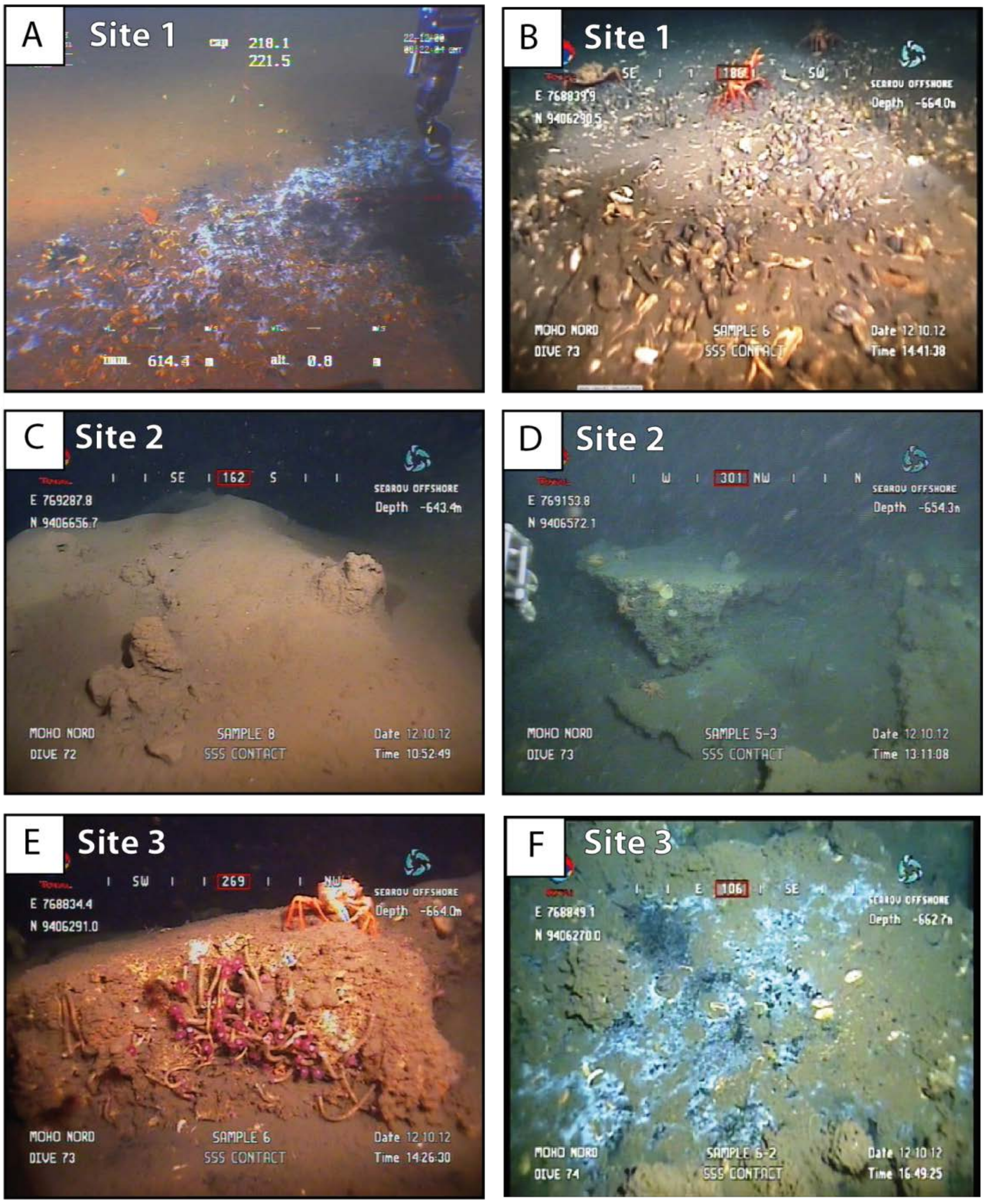
A
Site 1
B
Site 1
SERROU OFFSHORE
Depth -664.0m
MOHO NORD
DIVE 73
SAMPLE 6
SSS CONTACT
Date 12.10.12
Time 14:41:38
C
Site 2
E 769287.8
N 9406656.7
SERROU OFFSHORE
Depth -643.4m
MOHO NORD
DIVE 72
SAMPLE 8
SSS CONTACT
Date 12.10.12
Time 10:52:49
D
Site 2
E 769153.8
N 9406572.1
SERROU OFFSHORE
Depth -654.3m
MOHO NORD
DIVE 73
SAMPLE 5-3
SSS CONTACT
Date 12.10.12
Time 13:11:08
E
Site 3
E 768834.4
N 9406291.0
SERROU OFFSHORE
Depth -664.0m
MOHO NORD
DIVE 73
SAMPLE 6
SSS CONTACT
Date 12.10.12
Time 14:26:30
F
Site 3
SERROU OFFSHORE
MOHO NORD
DIVE 74
SAMPLE 6-2
SSS CONTACT
Date 12.10.12
Time 16:49:25

Fig.11:

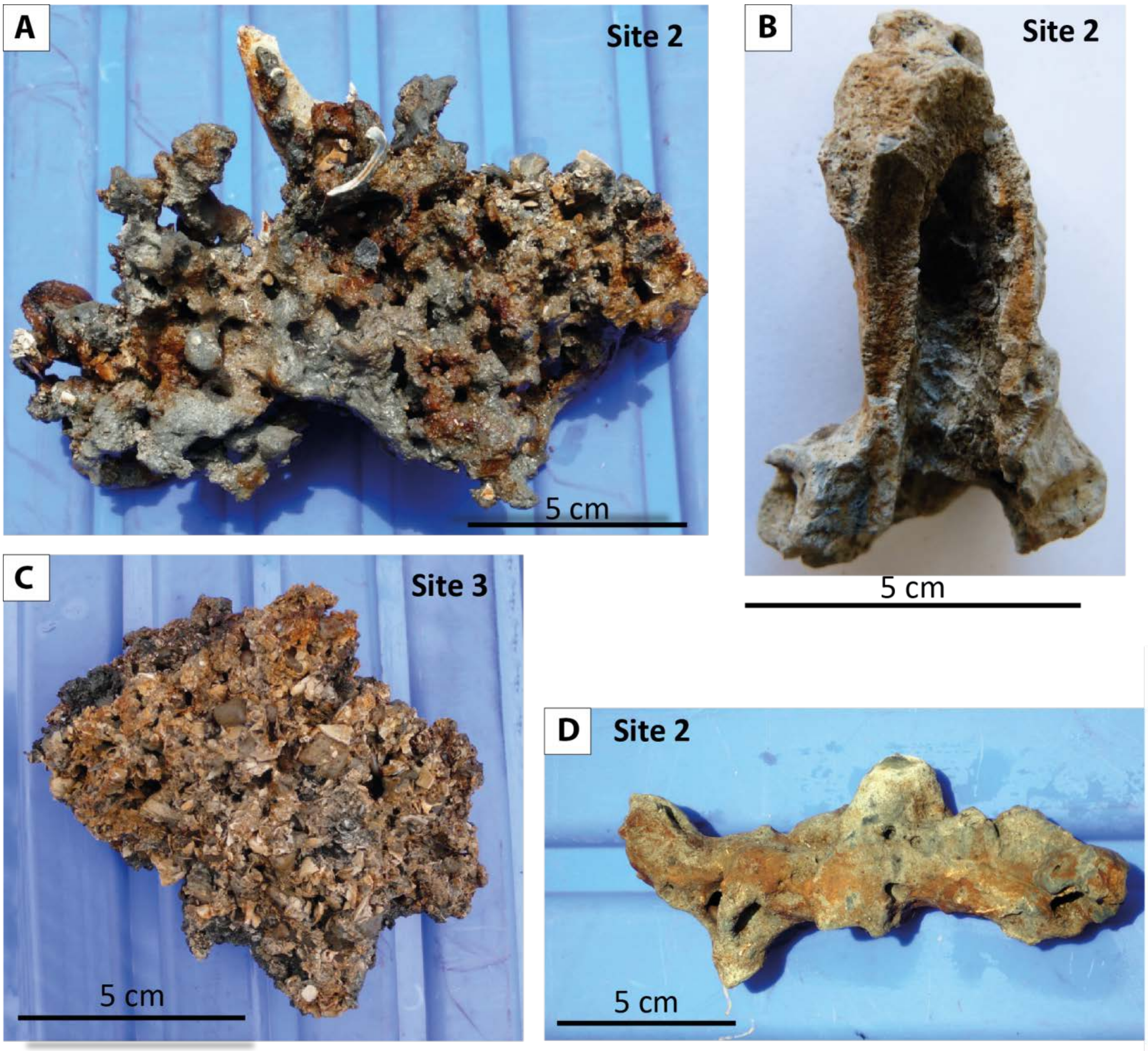

Fig.12:

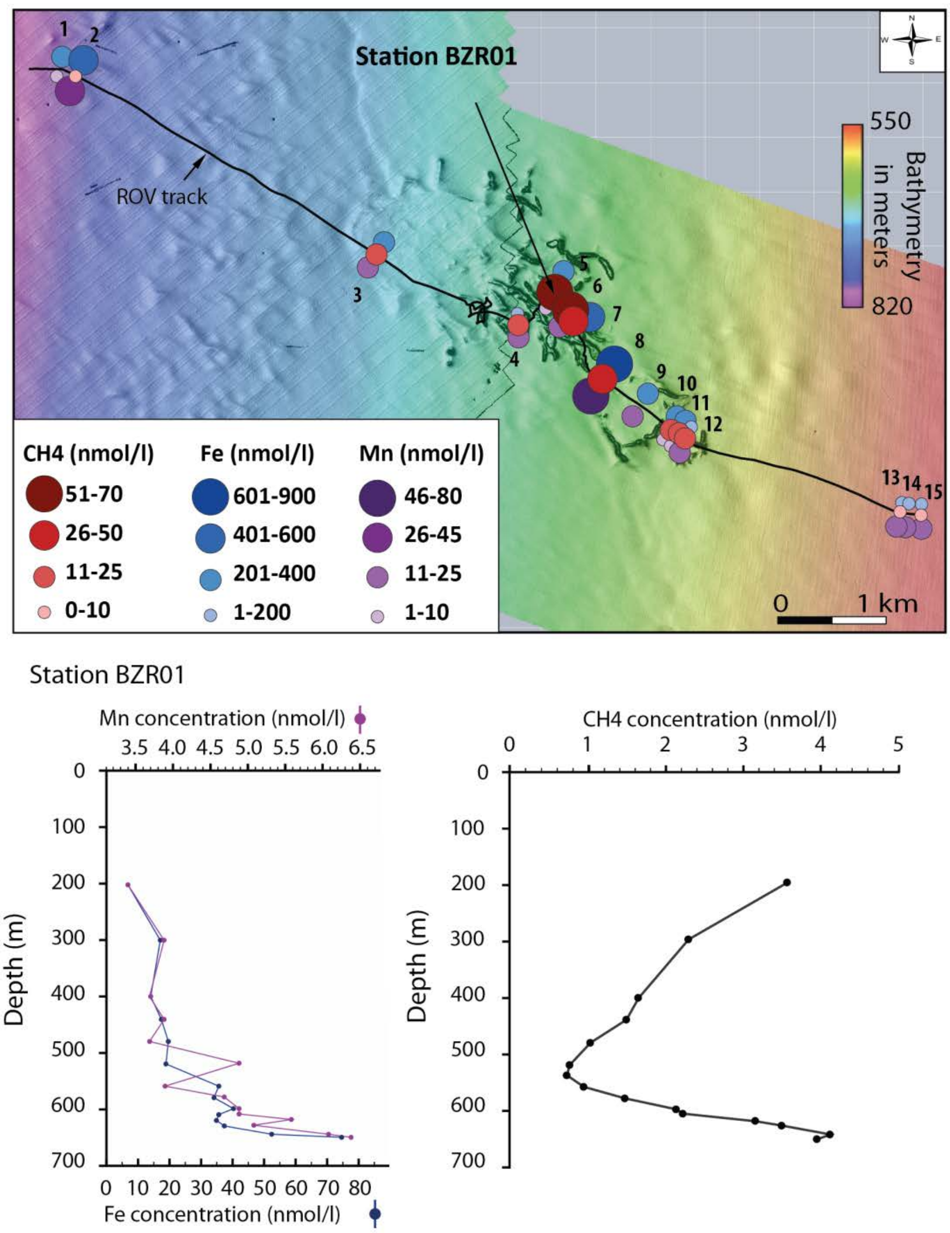

Station BZR01
ROV track
550
820
Bathymetry in meters
CH4 (nmol/l)
51-70
26-50
11-25
0-10
Fe (nmol/l)
601-900
401-600
201-400
1-200
Mn (nmol/l)
46-80
26-45
11-25
1-10
0
1 km
Station BZR01
Mn concentration (nmol/l)
3.5 4.0 4.5 5.0 5.5 6.0 6.5
Depth (m)
Fe concentration (nmol/l)
0 10 20 30 40 50 60 70 80
CH4 concentration (nmol/l)
0 1 2 3 4 5
Depth (m)

Fig.13:

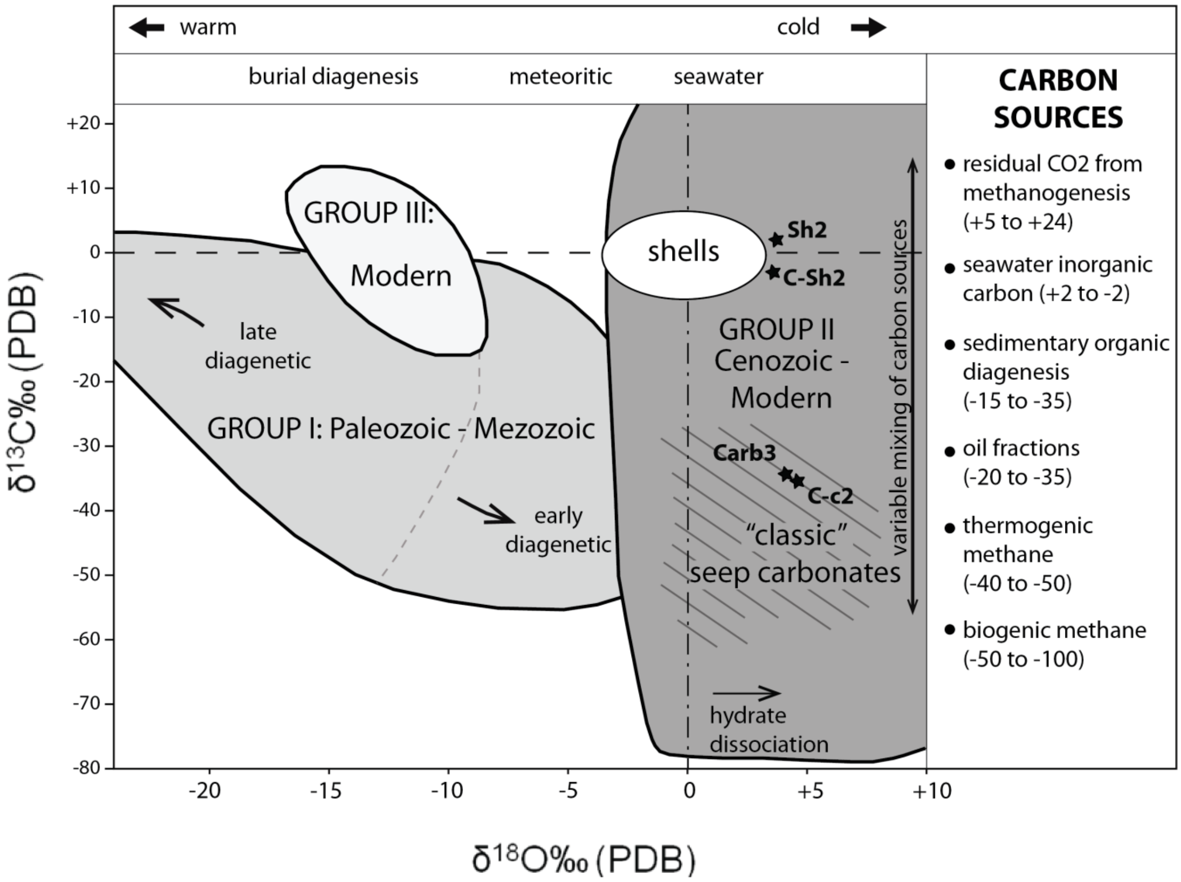
warm
cold
burial diagenesis
meteoritic
seawater
CARBON SOURCES
residual CO2 from methanogenesis (+5 to +24)
seawater inorganic carbon (+2 to -2)
sedimentary organic diagenesis (-15 to -35)
oil fractions (-20 to -35)
thermogenic methane (-40 to -50)
biogenic methane (-50 to -100)
GROUP III: Modern
shells
Sh2
C-Sh2
late diagenetic
GROUP II Cenozoic - Modern
GROUP I: Paleozoic - Mezozoic
Carb3
C-c2
"classic" seep carbonates
early diagenetic
variable mixing of carbon sources
hydrate dissociation
+20
+10
0
-10
-20
-30
-40
-50
-60
-70
-80
-20
-15
-10
-5
0
+5
+10
δ13C‰ (PDB)
δ18O‰ (PDB)

1546 Fig.14:

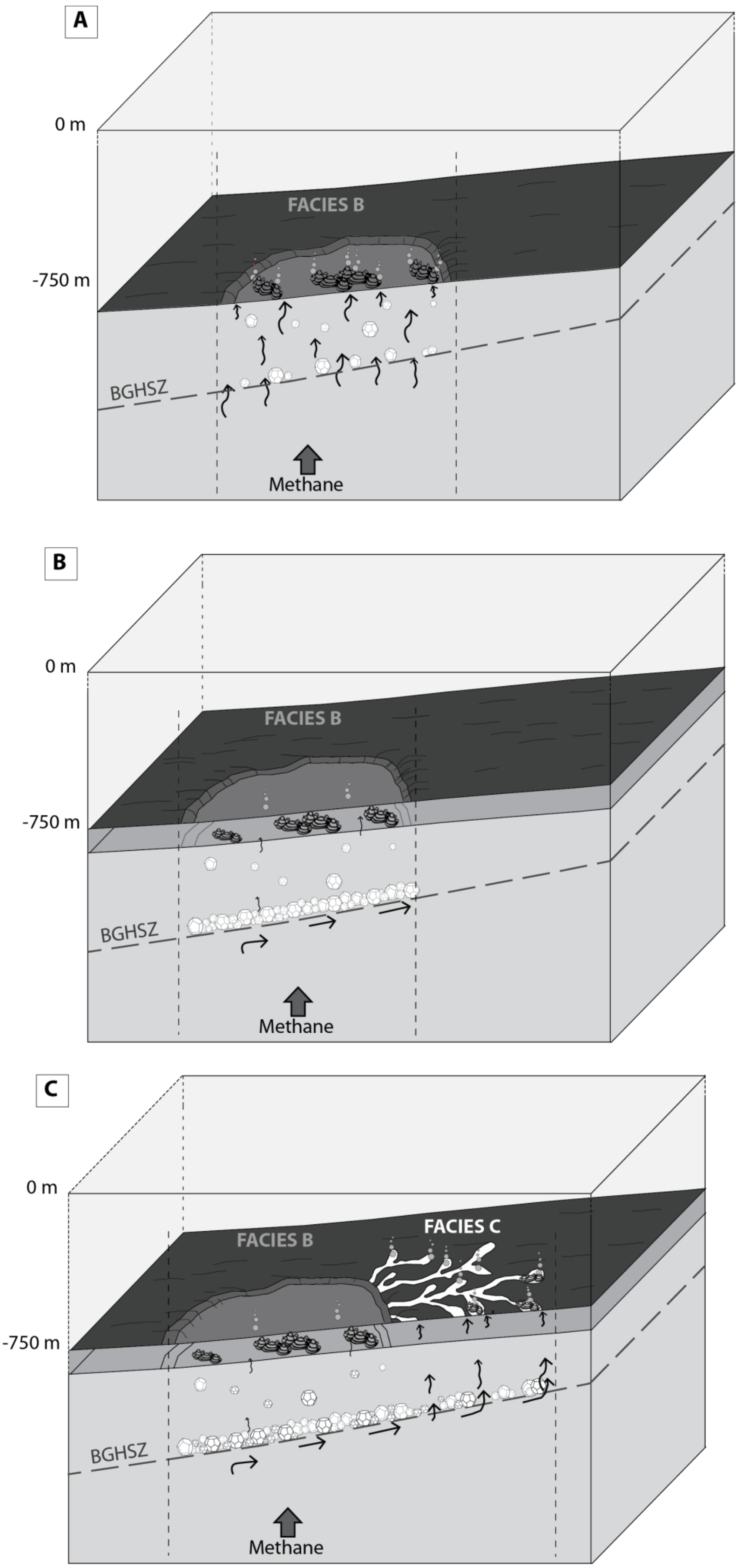

1547

Table 1:

	Samples	δ ^{13}C (PDB)	δ ^{18}O (PDB)	CaCO3 (%)
Site 2	Carbonate Cement fraction (**C-c2**)	-35,5	4,3	75,3
	Carbonate Shell fraction (**C-Sh2**)	-3,1	3,6	89,3
	Bivalve Shell (**Sh2**)	2,1	3,7	94,5
Site 3	Carbonate sample (**Carb3**)	-34,3	4,1	74,4

Table 2:

A. Hydrocats BZR01 samples:

Depth (m)	653	646	630	620	610	600	580	560	540	520	480	440	400	300	200	
CH4 (nmol/l)	3,9	4,1	3,4	3,1	2,2	2,1	1,4	0,9	0,7	0,8	1	1,5	1,6	2,3	3,5	
Fe (nmol/l)	75,1	52,8	37,7	35,3	36,1	40,9	34,5	36,1		19,3	20,1	17,8	14,6	17,8	7,4	
Mn (nmol/l)	6,4	6,1	5,1	5,6	4,9	4,9	4,7	3,9		4,9	3,7	3,9	3,7	3,9	3,4	3

B. ROV water samples :

Num d'ech (Zaïrov)	1	2	3	4	5	6	7	8	9	10	11	12	13	14	15
Seismic morphotypes	MA	MA	MB	MC	MC	MC	MC	MC	MB	MC	MC	MC	MA	MA	MA
CH4 (nmol/l)		3	16	23	70	68	42	43		18	20	24	6		3
Fe(nmol/l)	309	597	278	185	287		436	867	222	265	234	188	185	188	154
Mn (nmol/l)	9	45	17	13	3		21	74	13	9	6	14	17	11	11
Si (µmol/l)	22	39	40	35	35	36	36	36	33	33	32	33	32	31	31